NANO · MICRO small
www.small-journal.com

One-Step Tunable Human Hair Keratin Gradient Hydrogel with Antibacterial Activity for Tissue Engineering

*Marin Zhen Lin Yee, Yun Wei Lim, Logeshwari Muthualagu Natarajan, Bertrand Czarny, and Kee Woei Ng**

Gradient hydrogels are an emerging strategy in tissue engineering to mimic the heterogeneity in native tissues. Herein, the metal-thiolate complexation mechanism is exploited by allowing diffusion of silver ions (Ag^+) through a cysteine-rich human hair keratin (HHK) solution to produce a novel gradient hydrogel. This one-step approach enables the combined benefits of a sustainable material with an established antimicrobial agent. Herein, the gelation kinetics, physical, mechanical, and biochemical properties of the gradient hydrogel are correlated over a range of thiol:Ag ratios. The presence of a porosity gradient within a single construct, along with dissimilar top and bottom surface morphologies, is shown. Disk diffusion tests against *Staphylococcus aureus* verified the antibacterial activity of this Ag-loaded hydrogel. Additionally, hydrogels at 1.25 thiol:Ag ratio supported > 95% viability and proliferation of human dermal fibroblasts (HDFs), comparable to collagen hydrogels. These HDFs produce fibronectin, collagen III, and express alpha-smooth muscle actin within the gradient hydrogels. In an in vivo full-thickness wound healing mouse model, the 1.25 hydrogel evoke minimal host tissue response, support reepithelialization more than the uniform Gelatin Methacrylate (GelMA) hydrogel, and promote the most collagen deposition. These findings demonstrate the practicality of metal-thiolate complexation in producing biomimetic gradient hydrogels for tissue regeneration.

1. Introduction

Human hair keratins (HHKs) are naturally occurring biopolymers that have been utilized to develop hydrogel scaffolds due to the presence of multiple functional groups that give rise to various chemical coordination possibilities. Their propensity to form fibrous networks provides further structural support in a polymeric matrix. Out of 17 known HHK subtypes, 12 possess the cell adhesion motif LDV (leu-asp-val), which is recognizable by $\alpha_4\beta_1$ integrin.[1] As such, the application of HHK-based templates as an active substrate for tissue engineering has been explored over the years.[2–5] When compared to animal-derived biopolymers such as collagen or gelatin, HHKs mitigate the risks of interspecies pathogen transfers.[6] Moreover, derived from hair waste, HHKs are easily accessible, abundant, and have the potential to become a sustainable biomaterial resource.[7]

One unique feature of HHKs is their naturally occurring high cysteine content,[8] allowing the exploitation of disulfide bonds

M. Z. L. Yee, Y. W. Lim, L. Muthualagu Natarajan, B. Czarny, K. W. Ng
School of Materials Science and Engineering
Nanyang Technological University
Singapore 639798, Singapore
E-mail: kwng@ntu.edu.sg
M. Z. L. Yee
Health Technologies
Interdisciplinary Graduate Program
Graduate College
Nanyang Technological University
Singapore 637460, Singapore
The ORCID identification number(s) for the author(s) of this article can be found under https://doi.org/10.1002/smll.202509775
B. Czarny
Lee Kong Chian School of Medicine
Nanyang Technological University
Singapore 639798, Singapore
K. W. Ng
Nanyang Environment and Water Research Institute
Nanyang Technological University
1 Cleantech Loop, CleanTech One, Singapore 637141, Singapore
K. W. Ng
Skin Research Institute of Singapore
Clinical Sciences Building
11 Mandalay Road, Singapore 308232, Singapore

DOI: 10.1002/smll.202509775

as a means of gelation. For instance, by adjusting the pH of HHKs, Wang et al. fabricated a hydrogel through a pH precipitation method where keratin flocculates were stabilized through disulfide bonding. When implanted in a murine model, the hydrogel did not elicit an acute host tissue response.[3] Similarly, a HHK cryogel was formed through repeated freeze–thaw cycles that promote intermolecular cross-linking through disulfide bonding, hydrophobic interactions, and hydrogen bonding, giving rise to gelation. Unsuccessful cryogelation after the blocking of free thiols was demonstrated, emphasizing the important role that cysteines play in HHK gelation.[9] Instead of disulfide stabilization, it is also possible to leverage the thio-ene "click" reaction between the free thiols in HHKs and a 4-arm norbornene-functionalized polyethylene glycol photopatterned HHKs into cell-laden architectures of intricate designs.[4] Furthermore, HHK can readily form composites with other natural biopolymers, such as alginate, through the induction of amide bonds between the carboxyl and amine groups on both materials.[10] When employed as a dermal substitute to treat partial thickness burns in a porcine model, the HHK/alginate scaffold facilitated faster reepithelialization compared to untreated and collagen controls.[11]

HHK-based hydrogels developed by us and others have highlighted the versatility of HHKs, but the exploitation of metal ions as a cross-linker due to their high affinity to cysteines has yet to be explored. Hydrogels formed through metal-thiolate complexation can gel rapidly within seconds, giving rise to injectable hydrogels. These hydrogels are mainly made from the 4-arm thiolated polyethylene glycol ($(PEGSH)_4$)[12–15] or a synthetic thiolated bovine serum albumin.[16] There has been no documentation of gradient HHK hydrogels using metal-thiolate complexation. The human body is made up of various tissues and organs, each of which has unique distinguishing characteristics, such as cell type, biochemical constituents, orientation, etc. Yet these various parts collaboratively form a functioning organism. The interface, which is a region of transition between various tissues, plays a key role in this phenomenon. It usually exists with a gradient in cell types, mechanical stiffness, and microstructure, and this interface facilitates the co-maintenance of the tissues.[17] Therefore, gradient hydrogels, as compared to conventional hydrogels with uniform material properties, have received attention due to the possibility of mimicking these gradient interfaces with greater relevance.[18] Thus, studying the feasibility of producing a gradient hydrogel using HHKs, through interactions between metal ions and thiolates, could present new possibilities in the search for physiologically mimicking gradient hydrogels.

In this study, a novel gradient hydrogel is fabricated in a single step between HHKs and silver ions (Ag^+). This method takes advantage of the rapid gelation between the two components to induce an Ag^+ concentration gradient without the need for an interfacial permeable membrane. Through ionic diffusion, a HHK-Ag hydrogel with a continuous porosity gradient is established, which can be tuned by varying the mole ratio between the free thiols in HHKs and Ag^+ (thiol:Ag). The effect of this ratio on the gelation kinetics and subsequent material properties, such as mechanical strength, degradation profile, and water uptake capacity, was investigated. When the free thiols in HHK were fully blocked, an irregular construct was formed instead, emphasizing the importance of free thiols in the gradient gelation process. The hydrogel's gradient microstructure hinted at a possible application as a dermal template. Therefore, the suitability of the hydrogels to provide antimicrobial activity against the gram-positive *Staphylococcus Aureus* and support the proliferation of human dermal fibroblasts and their production of extracellular matrix proteins was evaluated. Their functionality as a dermal template was further verified in an in vivo full-thickness wound healing mouse model.

2. Results and Discussion

2.1. The Gradient Gelation of HHKs with Ag^+

To ensure that only keratins from the intermediate filaments (IF) fibers are collected, keratin-associated proteins (KAP) were first removed (Figure S1, Supporting Information). Keratins were subsequently extracted using a reductive method to break up the disulfide bonds, as visualized in its hierarchical structure (**Figure 1ai**). After dialyzing the keratin extracts against large volumes of deionized (DI) water for 24 h, the free thiol content in the human hair keratins (HHK) was 0.341 ± 0.034 mmol g^{-1} (Figure S2, Supporting Information). This value is comparable to that of a commercial thiolated polymer, $(PEGSH)_4$, at a theoretical range of 0.2–0.4 mmol g^{-1}.[12,13,19] To mitigate spontaneous oxidation, freshly dialyzed HHK solutions were prepared for all studies herein and utilized within two hours after conducting Ellman's assay. This is to ensure that as many thiols as possible are available for complexation with Ag^+. In addition, the HHKs maintained their characteristic α-helical secondary structure, the various protein amide bands, and the free thiol peak at 2558 cm^{-1} (Figure S3, Supporting Information) recorded using circular dichroism (CD) and Fourier transform infrared spectroscopy (FTIR), respectively, which align with the literature.[1,4,20]

The possibility of complexation between HHKs and Ag^+ was evaluated through transmission electron microscopy (TEM) to visualize their morphological interactions. A mixture of globular aggregates (⌀: 26.31 ± 7.49 nm) and short filamentous fragments was observed in samples of HHK in DI water (Figure S4a, Supporting Information). After Ag^+ addition (HHK-Ag), these short filamentous fragments elongated. Their mean diameter was measured to be 10.65 ± 1.65 nm (Figure S4b, Supporting Information), which is comparable to HHK nanofibers (8–10 nm) formed via self-assembly[21] and the characteristic 10 nm diameter of keratin IFs.[22] Also, the area percentage of globular aggregates decreased from 3.24% to 1.86% after Ag^+ addition (Figure S4c, Supporting Information). These interactions suggest the potential of HHKs forming nanofiber networks with Ag^+ through metal-thiolate complexation (Figure 1aii) and hence the feasibility of forming hydrogels at higher concentrations of both constituents.

The diffusion of Ag^+ into a HHK solution for gradient gelation requires the presence of a partially permeable membrane (PPM), and it is hypothesized that a thin PPM between the two can be formed without an external material support due to the high affinity between thiols and Ag^+.[23] As expected, the HHK solution gelled instantaneously upon contact with a silver nitrate ($AgNO_3$) solution. A thin HHK-Ag hydrogel layer is seen encapsulating the remaining HHK solution (Figure S5, Supporting Information). As such, a one-step fabrication process between

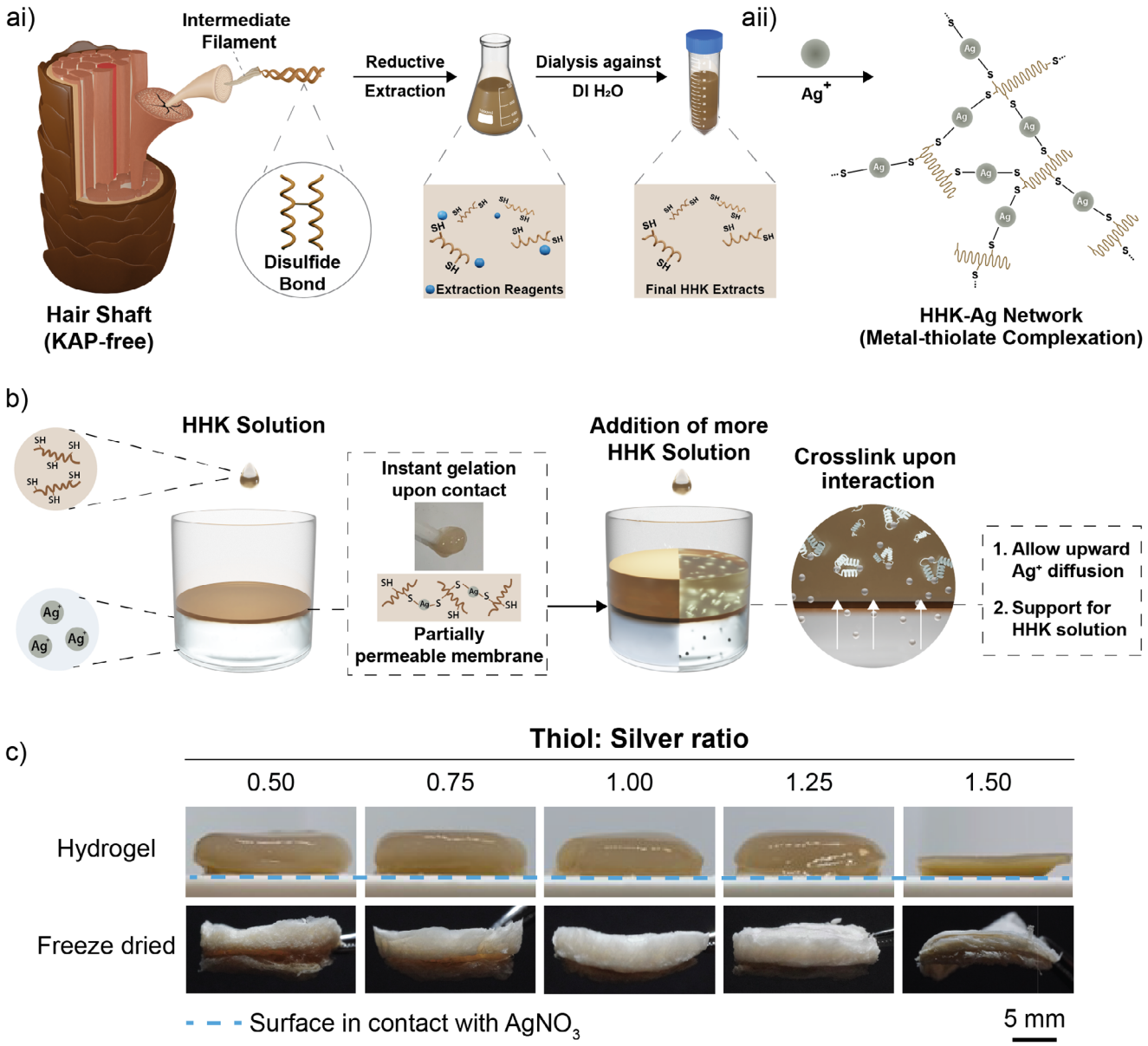

Figure 1. The tunable one-step fabrication process of HHK-Ag gradient hydrogels. ai) An illustration depicting the extraction of keratins from a human hair shaft devoid of keratin-associated proteins (KAP) and subsequent dialysis to obtain a final HHK extract. aii) A visualization of the HHK-Ag network formed via metal-thiolate complexation. b) An illustration depicting the fabrication of HHK-Ag gradient hydrogels. c) Gross optical images of the HHK-Ag gradient hydrogels and scaffolds formed over varying thiol:Ag ratios.

HHK and Ag^+ is established where the thin PPM was instantaneously formed by drop-casting a minute amount of HHK onto a $AgNO_3$ solution (Video S1, Supporting Information). This PPM supports the introduction of additional HHK solutions and facilitates the upward diffusion of Ag^+ into the HHKs (Figure 1b). As Ag^+ diffuses upward and complexes with HHKs, a gradient profile is created. The thiol:Ag mole ratios were varied (Table S1, Supporting Information) to modulate the gradient profile and subsequent hydrogel properties.

All parameters achieved complete gelation except the 1.50 hydrogel, where its supernatant contained HHKs at 10.13 ± 0.54 mg mL^{-1} with 3.43 ± 0.18 mM of free thiols (Figure S6, Supporting Information). This suggests that a minimal amount of Ag^+, between the 1.25 and 1.50 ratio, was required for complete gelation, defined as the gelation of the entire 1 mL of HHK solution. It was determined by ensuring there is no residual HHK solution after an overnight period of 16 h post-addition of HHK onto the ion bath. The gradient profile of the hydrogels was visually obvious after lyophilization (Figure 1c). The top region was light beige with a spongy texture, and the bottom region was dark brown with a flaky texture. The process of freeze–drying created an obvious interface between the two regions, which was not observable in the hydrogel state. Gradient hydrogels are often formed via layering isotropic hydrogels of

different materials or the same materials of varied properties.[24–26] Limitations of layering include time-consuming multiple steps, the need for complex apparatus setups, and the discontinuous junctions between adjacent layers. These junctions could become interfacial stress points and cause delamination when a load is applied.[18,27,28] Herein, these concerns are not applicable as only one biopolymer is used, and the gradient is produced in a single step due to the continuous diffusion and cross-linking process. Moreover, no external PPM or apparatus is required to induce Ag^+ diffusion. Other metal ions, such as zinc(II) and gold(III) ions could form the gradient hydrogel in the same manner (Figure S7, Supporting Information). However, due to the Ag^+-specific inherent antimicrobial activities and monovalency, Ag^+ was selected for this study.

2.2. The Gelation Kinetics of HHK-Ag Gradient Hydrogels Depend on the Thiol:Ag Ratio

To verify the role of Ag^+ as the cross-linker, temporal quantification of Ag^+ was conducted with Inductively Coupled Plasma Optical Emission Spectroscopy (ICP-OES) at 3 timepoints (Figure S8a, Supporting Information). A decrease in Ag^+ concentration was recorded at the onset of gelation for all thiol:Ag ratio samples, suggesting a rapid complexation process between Ag^+ and HHKs that led to the formation of the thin PPM layer. Continuously, the Ag^+ decreased steadily and significantly overnight (Figure S8b, Supporting Information). These results support the notion of an upward Ag^+ diffusion through the PPM into the HHK solution for the metal-thiolate complexation process and subsequent gelation.

The diffusion-mediated gelation kinetics were quantified with Turbiscan Lab (**Figure 2a**); a colloidal stability analyzer, as demonstrated previously.[29] Unlike others who use an external material such as a filter paper[30] or dialysis membrane[29] as the PPM, the PPM formed between HHKs and $AgNO_3$ as an integral portion of the hydrogel itself enables the interface between the two to be well-defined as gel thickness = 0 mm (Figure 2b). As the Ag^+ diffuses upward into the HHK, the movement of the gel front is identified as a sharp increase in T % due to the difference in refractive indexes between the hydrogel and the remaining HHK solution, along with the clear reduction of T % in the gelled region. Based on the gel thickness plotted as a function of time (Figure 2ci), the apparent diffusion coefficient of the gel front (D_{app}) was calculated with Equation (1). The results revealed that as the thiol:Ag ratio decreases from 1.25 to 0.50, the initial Ag^+ concentration increases, creating a greater Ag^+ concentration gradient and larger Ag^+ flux, thus decreasing the time required for complete gelation, reflected as an increase in D_{app} (Figure 2cii; Table S2, Supporting Information), which is consistent with other studies using a different material and ion valency.[29,31,32] Besides, the analyzer provides a colored profile of the changes in T % and BS % fraction in the HHK-Ag hydrogel as a function of time (Figure 2d). At any instance in the gelation profile, the fraction of BS % decreases as the thiol:Ag mole ratio increases from 0.50 to 1.50 due to less Ag^+ that was available for cross-linking, resulting in the differential visual gelation profiles as shown in Figure 2d. These results demonstrated the feasibility of using the Turbiscan Lab analyzer for the quantification of upward gradient gelation kinetics. Due to incomplete gelation in the 1.50 hydrogel, it was excluded from subsequent analyses.

2.3. The Importance of Free Thiols in HHK to Form a HHK-Ag Gradient Hydrogel

The silver–thiolate (Ag—S) bonds are postulated to be responsible for cross-linking the HHKs to form the gradient hydrogel. For verification, the 1.00 hydrogel was selected due to the equimolar addition of Ag^+. FTIR analysis detected the presence of thiols at 2558 cm^{-1} in HHK but not in HHK-Ag hydrogel (Figure S9, Supporting Information), suggesting Ag—S complexation.[33] Based on X-ray Photoelectron Spectroscopy (XPS) (**Figure 3a**), Ag3d signals were present only on the bottom surface of the gradient hydrogel (Figure 3bi), in which the Ag—S peak at 369.33 eV was specifically detected (Figure 3bii).[34,35] Ag3d signal on the top surface of the gradient hydrogel and in HHK was not detected, indicating the absence of Ag. In the S2p region, a binding energy shift was observed only on the bottom surface of the hydrogel (Figure 3ci). The free thiol peak was detected on the top surface of the hydrogel at 163.57 eV (Figure 3cii) and 163.92 eV in HHK (Figure S10, Supporting Information).[36,37] In contrast, on the bottom surface, the peak at 162.69 eV corresponds to thiols in a thiolated state (Figure 3ciii). This chemical shift from ≈163 to ≈162 eV is a hallmark of Ag—S formation, which is well reported in the literature.[36–38] These results corroborate the presence of Ag—S bonds in the HHK-Ag gradient hydrogel.

To prove the hypothesis that Ag—S bonds dominate in the gelation of the HHK-Ag gradient hydrogel, the free thiols in HHKs were deactivated with N-ethylmaleimide (NEM) at 10 molar excess. NEM reacts with free thiols to form an irreversible thioether bond, (NEM–HHK, Figure 3d), reducing the free thiol content of HHK by 98.67% from 0.355 to 0.005 mmol g^{-1} (Data not shown). Unlike the HHK, the NEM–HHK could not form the clean PPM but instead, NEM–HHK-Ag clumps were formed (Figure 3ei), resulting in a randomized microstructure (Figure S11, Supporting Information). Yet, a decrease in Ag^+ in the ion bath was recorded for the NEM-HHK-Ag despite complete thiol blocking (Figure 3eii). These results showed that gelation occurred even without thiols, albeit irregularly, indicating that Ag^+ had interacted with other entities such as carboxylic and amine side groups.[39,40] These results suggest a combinatory effect of Ag—S bonding and additional interactions involving Ag^+ that resulted in the HHK-Ag gradient hydrogels, in which free thiols are essential.

2.4. The Microstructure of the HHK-Ag Gradient Hydrogels is Tunable

The Turbiscan analysis demonstrated the effect of the thiol:Ag mole ratio on the gradient profiles presents in the hydrogels. Therefore, a tunable gradient microstructure is expected. A dissimilar surface topography was observed between the top and bottom surfaces of the 0.50 hydrogel (**Figure 4ai**) where the top surface was rough and slightly porous, and the bottom surface had no pores. Across the height of the hydrogel, a porosity gradient was produced where the bottom portion comprised large flat

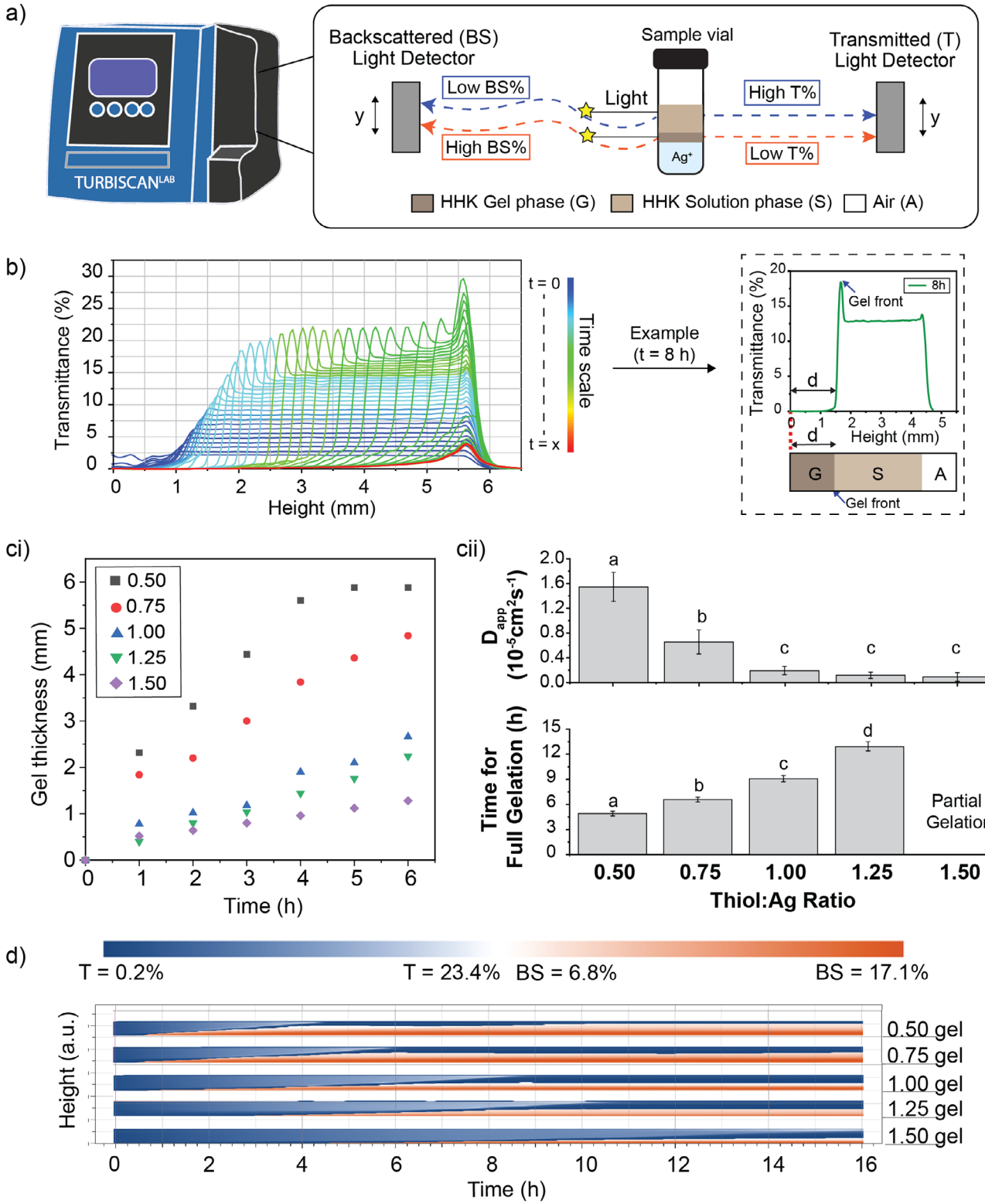

Figure 2. Quantifying gelation kinetics. a) An illustration depicting sample set-up and data acquisition in the Turbiscan Lab analyzer. b) Plot of the moving gel front as captured by Turbiscan and corresponding analysis approach to obtain the gel height at each time interval. ci) Gel thickness as a function of time with varied thiol:Ag mole ratios. cii) The established relationship between the apparent diffusion coefficient of the gel front (D_{app}), time required for gelation and the thiol:Ag ratio. Quantitative data presented as mean ± SD, n = 3. Samples labeled with different letters are statistically different at $p < 0.05$, One-way ANOVA with Tukey's post-hoc test. d) A gradient color profile reflecting the changes in T % and BS % across the sample height over 16 h for all samples.

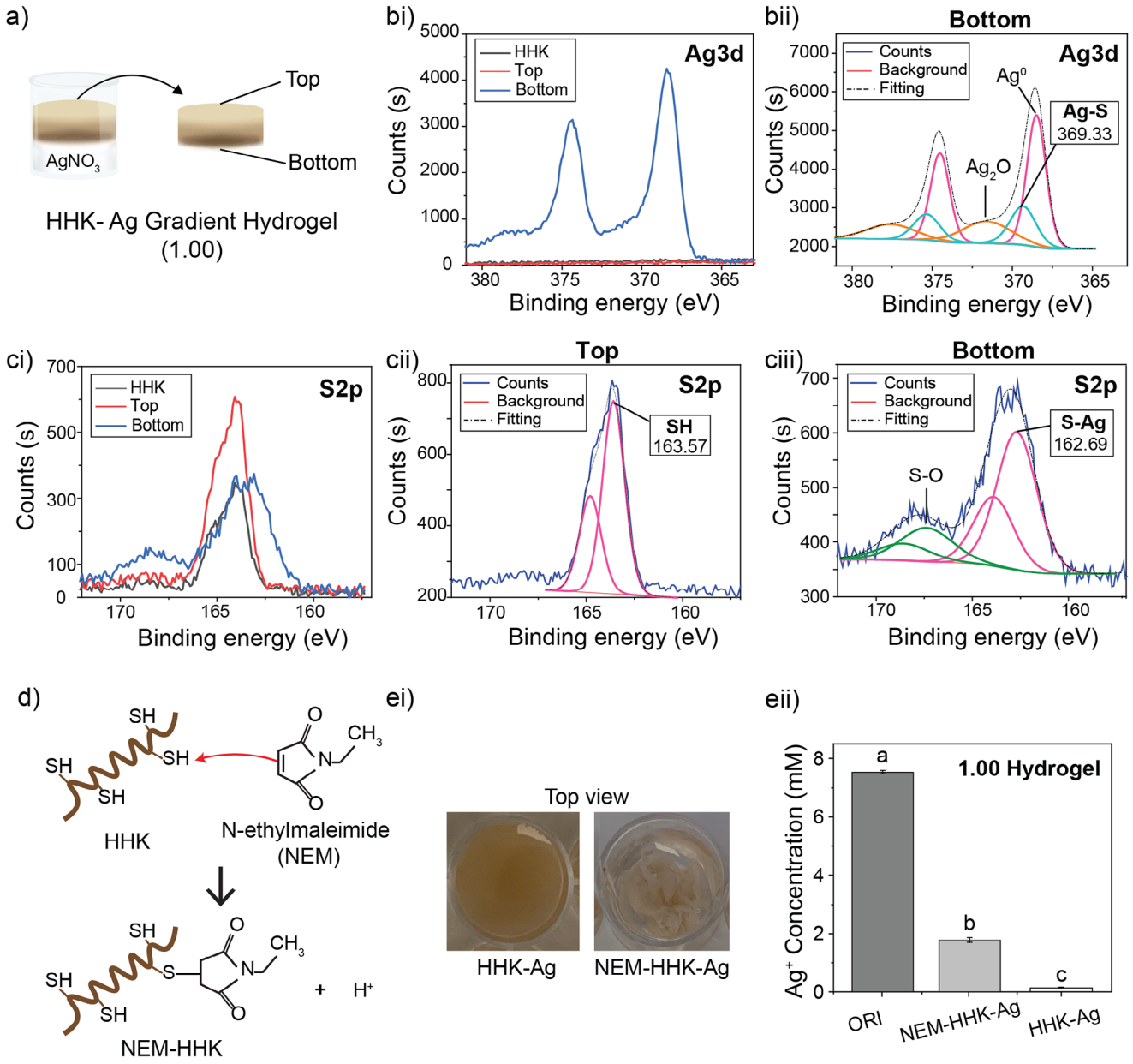

Figure 3. The significance of free thiols in the HHK-Ag gradient hydrogel. a) An illustration depicting the top and bottom surfaces of the 1.00 hydrogel in relation to XPS analysis. bi) Narrow scan XPS spectra of the HHK hydrogel in the Ag3d region. bii) Fitted Ag3d peaks of the bottom surface of the hydrogel, showing the Ag—S peak. ci) Narrow scan XPS spectra of the HHK hydrogel in the S2p region. cii) Fitted S2p peaks of the top surface of the hydrogel, showing the free thiol (SH) peak. ciii) Fitted S2p peaks of the bottom surface of the hydrogel, showing the S–Ag peak. d) An illustration depicting the blocking of thiols in HHK with N-ethylmaleimide (NEM). ei) Top-view images of HHK-Ag hydrogel and the irregular NEM–HHK-Ag construct. eii) Ag^+ concentration in the ion bath before the addition of HHK (ORI) and after the formation of the irregular NEM–HHK-Ag construct and HHK-Ag hydrogel. Quantitative data presented as mean ± SD, n = 3. Samples labeled with different letters are statistically different at $p < 0.05$, One-way ANOVA with Tukey's post-hoc test.

pores, and toward the top surface, smaller pores were present at a minor fraction (Figure 4aii). In addition, a nonuniform pore wall thickness was observed where the wall thickness of the large flat pores at 5.597 ± 1.89 µm was significantly greater than that of the smaller pores at 0.436 ± 0.15 µm (Figure 4aiii). These structural gradients were also present in the 1.25 hydrogel, but as a different profile. Similarly, the bottom surface had no pores, but the porosity of the top surface was observably higher (Figure 4bi). The 1.25 hydrogel had a steeper gradient in which the large flat pores at the bottom surface were present at a minor fraction, and moving upward, the pore size decreased over a range (Figure 4bii). As such, three regions instead of two could be defined in the 1.25 hydrogel pore distribution: top (0.350 ± 0.11 µm), middle (1.04 ± 0.56 µm), and bottom (6.09 ± 1.96 µm) (Figure 4biii).

The microstructural difference between the 0.50 and 1.25 hydrogels was attributed to the difference in the initial Ag^+

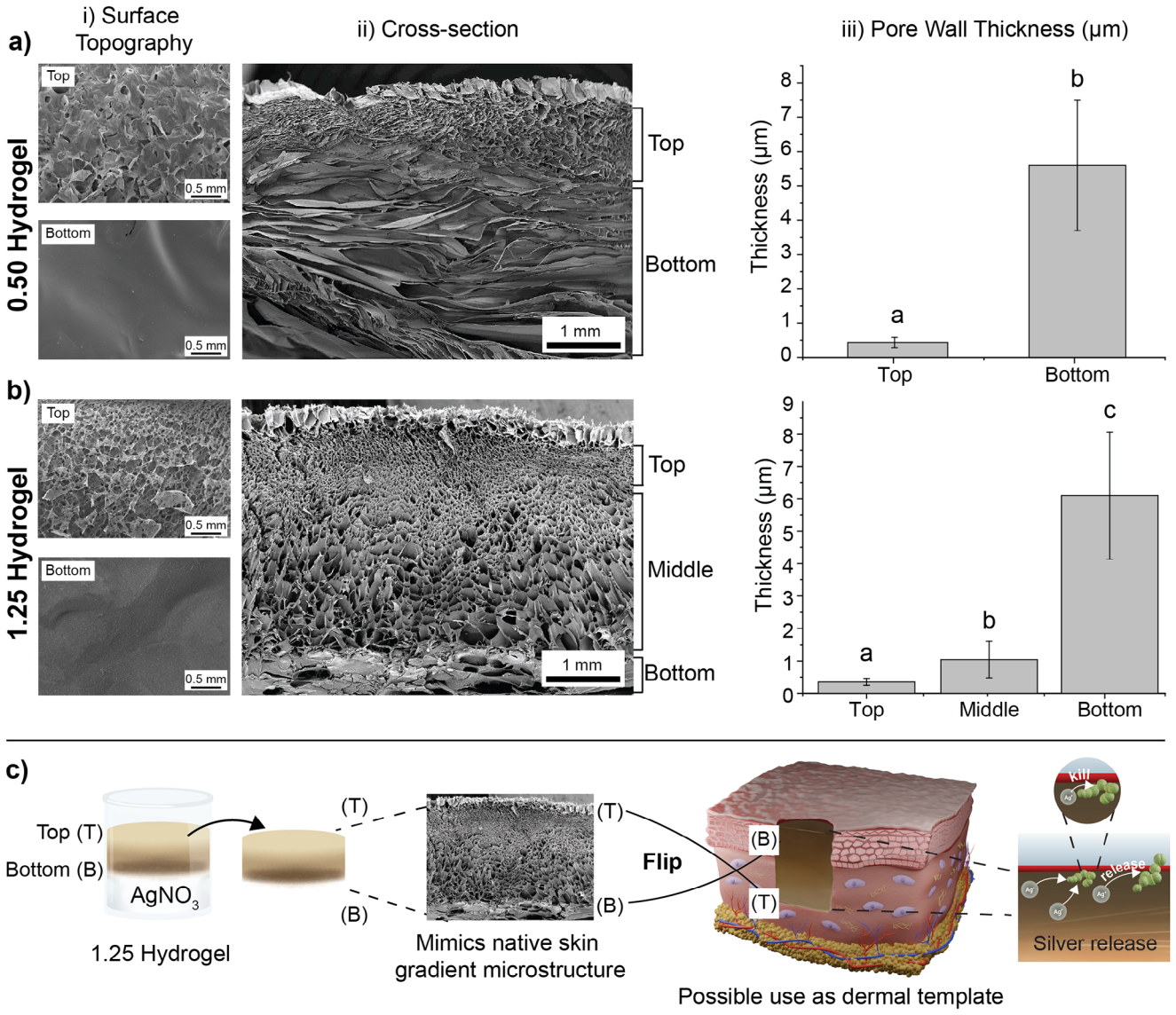

Figure 4. Microstructure of HHK-Ag gradient hydrogels. a) SEM images of the 0.50 hydrogel depicting the i) surface topography ii) cross-section, and iii) the average pore wall thickness in the top and bottom regions. b) SEM images of the 1.25 hydrogel depicting the i) surface topography ii) cross-section and iii) the average pore wall thickness in the top, middle, and bottom regions. c) An illustration to depict the possible application of the re-oriented 1.25 hydrogel as an antibacterial dermal template for wound healing. Quantitative data presented as means ± SD, n = 50. Samples labeled with different letters are statistically different at $p < 0.05$, One-way ANOVA with Tukey's post-hoc test.

concentration during fabrication, in which the 0.50 thiol:Ag mole ratio had a higher Ag^+ concentration. In reference to the Turbiscan color profile (Figure 2d), the BS % signal across the height of the 0.50 hydrogel continued to increase despite achieving full gelation after ≈5 h. This suggests a continuous diffusion of Ag^+ into the HHK solution as long as an ionic concentration gradient exists, resulting in an ongoing interaction with the HHK-Ag network via interactions as described earlier. Consequently, the 0.50 hydrogel, which had the highest content of Ag^+, comprised a higher fraction of the large flat pores with thicker walls, which would have interfered with light transmission during the Turbiscan analysis, resulting in higher backscatter signals as seen in Figure 2d. More importantly, these gradient features could be established in one single step, thus continuity between the pores was not disrupted, which helps to mitigate possible delamination between the pore layers. Also, the larger porosity gradient in the 1.25 hydrogel, alongside with the unique dissimilar topography, is favorable as the nonporous and porous surface mimics the epidermis and dermis of the native skin, suggesting its possible application as a dermal template for skin regeneration. When situated in the wound as illustrated in Figure 4c, the nonporous surface (B) faces the external environment, and the porous surface (T) faces into the dermis. Because the amount of Ag is greater toward surface B, it provides a targeted approach to mitigate bacterial influx from the external environment through controlled release of Ag^+.

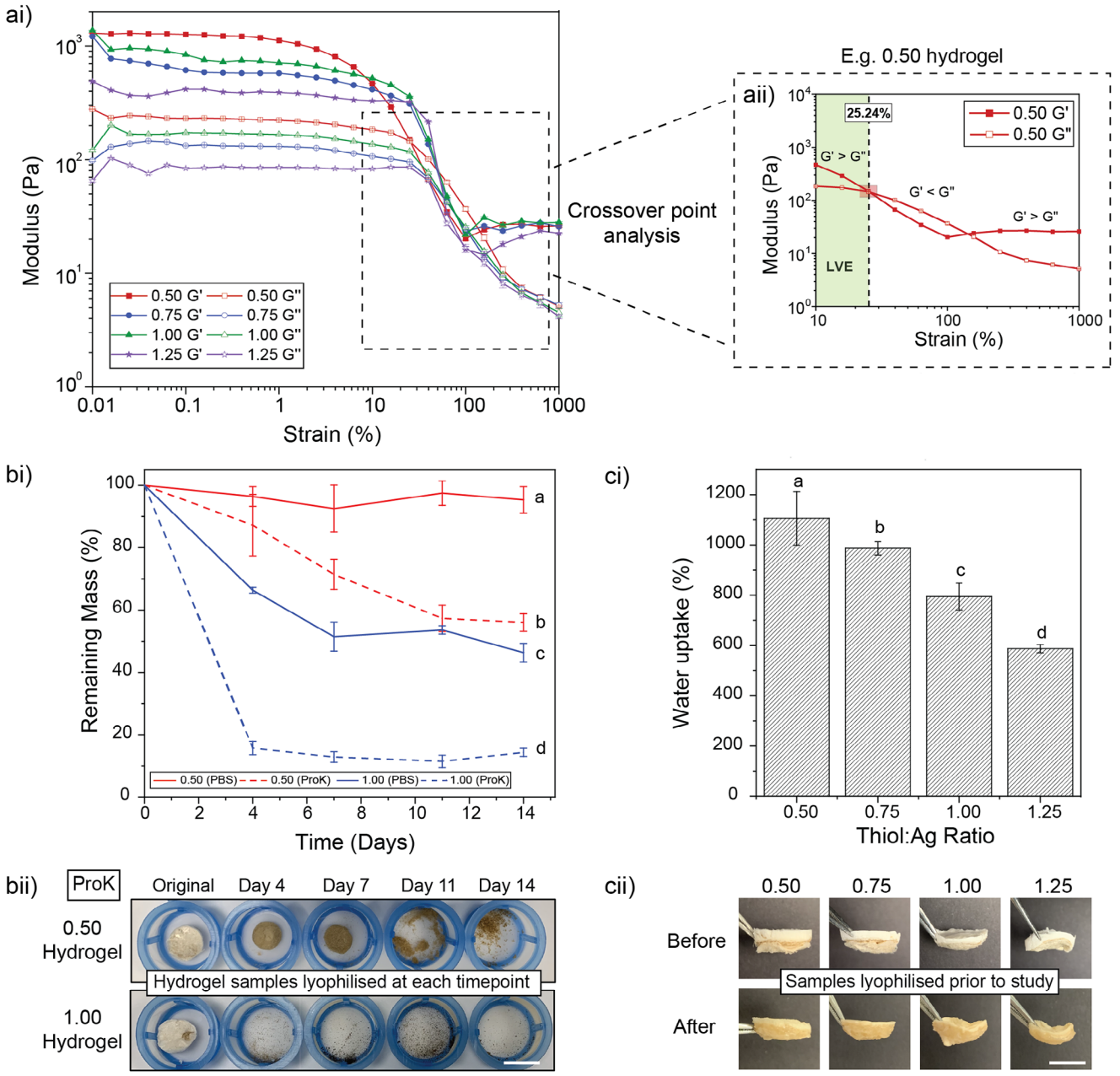

Figure 5. Material characterization of the HHK-Ag gradient hydrogels. ai) Oscillatory amplitude sweep test conducted on the HHK-Ag gradient hydrogels at varied thiol:Ag mole ratios. aii) A zoom-in view of the crossover point using the 0.50 hydrogel as an example. The linear viscoelastic region (LVE) in the plot is shaded in green. bi) The remaining mass profile of the 0.50 and 1.00 hydrogel across 14 days in the presence of ProK and PBS. Data presented as mean ± SD, n = 6. bii) Images of the 0.50 and 1.00 hydrogels lyophilized at each timepoint after being subjected to 0.5 U mL^{-1} Proteinase K (ProK) degradation. Scale bar: 20 mm. ci) Water uptake (%) of the HHK-Ag gradient hydrogels at varied thiol:Ag mole ratios. cii) Images of HHK-Ag Gradient hydrogels before and after water uptake in the top, bottom, and side view for all thiol:Ag mole ratios. Scale bar: 10 mm. Quantitative data represented as means ± SD, n = 5. Samples labeled with different letters are statistically different at $p < 0.05$, One-way ANOVA with Tukey's post-hoc test.

2.5. Microstructure-Dependent Material Properties of the HHK-Ag Gradient Hydrogels

The mechanical properties of the HHK-Ag gradient hydrogels were characterized with an oscillatory amplitude sweep test. The storage modulus (G') and loss modulus (G'') of the gradient hydrogels improved as more Ag^+ was incorporated during gelation (lower thiol:Ag mole ratio), with the lowest G' value recorded at 416.33 ± 0.05 Pa in the 1.25 hydrogel and the highest G' value of 1228.33 ± 0.26 Pa in the 0.50 hydrogel (**Figure 5**ai). For comparison, the G' value of native skin was reported to be between 361.9 ± 93.7 to 447.7 ± 119.2 Pa,[41] and 1160 Pa for a commercial wound dressing, IntegraDRT.[42] These values are close to the G' values of the HHK-Ag gradient hydrogels, suggesting

their suitability as dermal templates from a mechanical standpoint. With correlation to their microstructure, the higher fraction of large flat pores with thicker walls in the 0.50 hydrogel compared to that of the 1.25 had likely contributed to the higher amount of elastic energy the hydrogel could store prior to deformation. One interesting observation was that the G′ values exceeded the G″ values beyond the linear viscoelastic (LVE) region across all sample groups (Figure 5aii). This was different from reported literature for non-gradient isotropic hydrogels, where beyond the crossover point, G'' becomes greater than G', indicating shear-thinning and deformation.[14] This was likely due to the nonuniform porosity and pore wall thickness in the gradient hydrogel, which led to nonuniform mechanical properties and differential deformation kinetics across the height of the sample during the amplitude sweep test. Comparing the crossover values, the sample groups can be arranged in the ascending order of 0.50 < 0.75 < 1.00 < 1.25 (Table S3, Supporting Information). Conventionally, an isotropic hydrogel with greater G' and G'' will reach a crossover point at a higher strain value.[9] Yet, the 0.50 hydrogel had the highest G' and G'' among the hydrogels, but the lowest crossover point strain value of 25.24%. This could be due to the highest nonuniformity in the gradient profile of the 0.50 hydrogel as reflected in the Turbiscan profile (Figure 2d).

The uniaxial compression test on the gradient hydrogels demonstrated gradient microstructure-dependent mechanical properties as well, in which the 0.50 hydrogel had the highest compressive modulus of 2.18 ± 0.04 kPa, and for the 1.25 hydrogel, a modulus of 1.30 ± 0.09 kPa was recorded (Figure S12, Supporting Information). The higher fraction of the large flat pores with thicker walls in the 0.50 hydrogel compared to the 1.25 hydrogel was likely to have rendered the 0.50 hydrogel with a higher compressive modulus. Better mechanical properties of scaffolds due to thicker pore walls have been reported by others as well.[43,44] Nonetheless, the compressive strength for the 0.50 hydrogel was 50.54 ± 7.16 kPa, which was significantly lower than the 1.25 hydrogel at 190.57 ± 44.93 kPa. Isotropic hydrogels with higher compressive modulus are reported to withstand higher compressive strength.[45]

Other material properties, such as degradation, were studied in PBS (pH 7.4) and Proteinase K (ProK, 0.5 U mL^{-1}) for hydrolytic and enzymatic degradation, respectively, for the 0.50 and 1.00 gradient hydrogels. The remaining mass calculated by Equation (2) by day 14 for 0.50 hydrogel and 1.00 hydrogel in the presence of ProK was 56.02 ± 2.81% and 14.39 ± 1.31% respectively. Both hydrogels retained higher mass when subjected to only hydrolytic degradation in PBS (**Figure 5**bi). The difference in their respective degradation profiles was reflected in the images of the lyophilized hydrogels at each timepoint as well (Figure 5bii). The SEM images in Figure 4a and the Turbiscan profile in Figure 2d suggested that the 0.50 hydrogel had a larger fraction of large flat pores with thicker walls compared to the 1.00 hydrogel. A thicker pore wall would correlate to a denser hydrogel network, thus hindering the enzymatic cleavage of the peptide bonds or the hydrolytic degradation.[46] Also, a larger pore size would reduce the surface area-to-volume ratio for the ProK to act on and PBS to interact with.[47] Collectively, this will retard the rate of degradation in the 0.50 hydrogel. Another microstructure-dependent property evaluated is the water uptake capacity of the gradient hydrogel scaffolds (Equation 3). It was observed that as the thiol:Ag mole ratio decreased from 1.25 to 0.50, the scaffolds' water uptake capacity increased from 587.05 ± 16.35% to 1106.06 ± 106% (Figure 5ci), and the amount of scaffold warpage decreased (Figure 5cii). A pore of larger size would be able to uptake more water,[48] and the 0.50 scaffold had the highest fraction of large flat pores. The 0.50 scaffold experienced the least warpage due to the smallest porosity gradient across the scaffold height, leading to the lowest nonuniformity in water uptake. These studies have shown that by simply modulating the thiol:Ag mole ratio during fabrication, the microstructure profile of the gradient hydrogel can be controlled, resulting in tunable material properties.

2.6. HHK-Ag Gradient Hydrogels Function as an Antibacterial Template

To verify the antibacterial properties of the HHK-Ag gradient hydrogels, the Kirby–Bauer disk diffusion test was conducted. With the gradient microstructure indicating the possible use of the hydrogels as a dermal template, the Gram-positive *Staphylococcus aureus* present dominantly in wounds[49] was selected for the test, at the physiologically relevant concentration[50] of 2.4×10^8 CFU mL^{-1}. The inhibition zones created by the 0.50 and 1.25 hydrogels were measured to be 20.21 ± 0.94 and 16.43 ± 0.28 mm, respectively (**Figure 6**a). This was expected as the Ag^+ concentration used in the fabrication of 0.50 hydrogel was significantly higher than that of the 1.25 (mole ratio of free thiols in HHK to Ag^+). Contrary, the HHK solution as a negative control did not record a zone of inhibition. These results verified the role of Ag^+ as both a hydrogelator and antibacterial agent when complexed with HHKs in the gradient hydrogel.

2.7. The HHK-Ag Gradient Hydrogels can be Tuned to Support Cell Viability and Proliferation

Excessive Ag leaching from the Ag-based hydrogels could impose a cytotoxic effect and needs to be systematically evaluated. To do this, the 50% cytotoxic concentration (CC_{50}) of $AgNO_3$ against human dermal fibroblasts (HDFs) was first determined to be 19.32 ± 2.48 µM (Figure S13, Supporting Information), which is in close agreement with others.[51] When the hydrogels were immersed in supplemented DMEM (Figure S14a, Supporting Information), the concentration of Ag^+ in the leachates across the hydrogel groups had no significant differences (Figure 6b) on days 1, 3, 5, and 7 despite a difference in the amount of Ag^+ used for their fabrication. Also, the cumulative leached amount (Equation (4)) was highest at only 0.73% by day 7 (Figure S14b, Supporting Information). Moreover, the leachate concentrations were not significantly different in the presence of HDFs cultured on the hydrogels (Figure S14c, Supporting Information), suggesting that the Ag leachates recorded could be due to the diffusion of unbound Ag^+ or Ag complexes that were trapped within the hydrogel post-washing. Regardless, when compared to the CC_{50} value, these leachates can be deemed as noncytotoxic.

To validate the possible use of the HHK-Ag gradient hydrogels as a dermal substrate for tissue regeneration, their fundamental ability to support HDF attachment, spreading, and proliferation was assessed. The metabolic activity of the HDFs was quantified

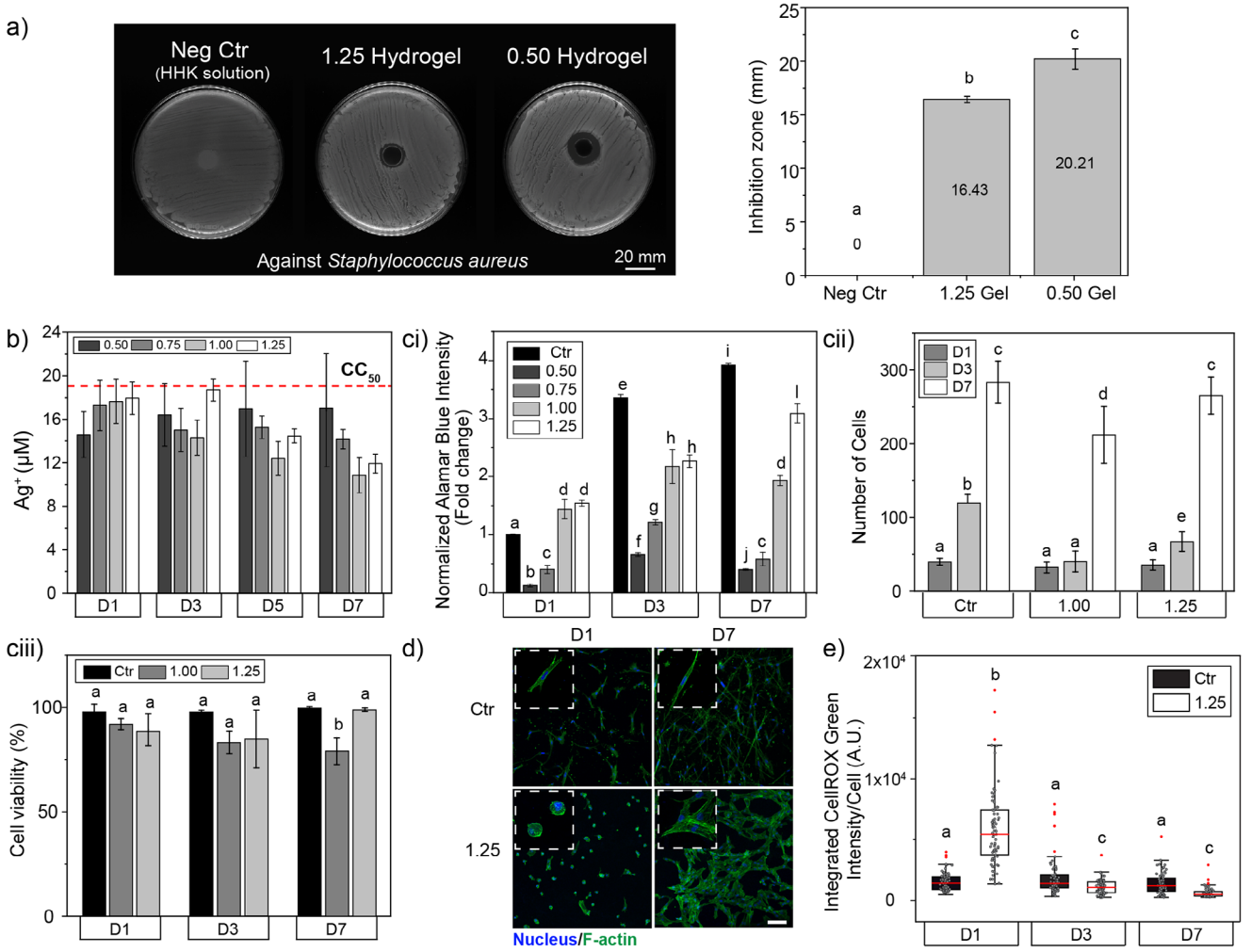

Figure 6. Evaluation of the antibacterial properties and cytocompatibility of the HHK-Ag gradient hydrogels. a) Kirby–Bauer disk diffusion test showcases the tunable antibacterial properties of the hydrogels against *Staphylococcus aureus* (n = 3). b) Concentrations of Ag leachates from the hydrogels at all time points were found to have no differences between sample groups and were all generally lower than the CC_{50} value of $AgNO_3$ against HDFs (n = 3). ci) Metabolic activity of the cultured HDFs, measured through the Alamar blue assay, was highest for the 1.25 hydrogel on day 7 amongst the HHK-Ag gradient hydrogels (n = 3). cii) The 1.25 hydrogel supports HDF proliferation comparably to the control, determined by count analysis of Hoechst-stained cells (n = 3). ciii) Cell viability of HDFs cultured on day 7 was beyond 98% for both the control and 1.25 hydrogel, determined by propidium iodide and Hoechst staining (n = 3). d) CLSM images demonstrate substrate compatibility of both the control and 1.25 hydrogel, in which HDFs could attach and spread into a spindle-like morphology. The white box demarcates a zoom-in region of the HDF cultures. Scale bar: 100 μm. e) The 1.25 hydrogel does not induce oxidative stress on the cultured HDFs based on the CellROX assay. For all boxplots, the minimum and maximum boundary lines represent the 25th and 75th percentile values, respectively. The median value is presented by the red line. Both top and bottom whiskers represent the 1.5SD limits, and outliers in red were excluded from the statistical analysis (n = 75). All quantitative data are presented as means ± SD. Samples labeled with different letters are statistically different at $p < 0.05$; One-way ANOVA with Tukey's post-hoc test or two-tailed Student's *t*-test was adopted.

with the Alamar blue assay, and among the HHK-Ag gradient hydrogel groups, HDFs cultured on the 1.25 samples had the highest metabolic activity by day 7 of culture (Figure 6ci). The 1.25 hydrogel could support cell proliferation comparably to the type 1 collagen hydrogel control, as indicated by the continuous increase in metabolic activity across the timepoints, corresponding to increasing cell numbers determined by Hoechst nuclei stains (Figure 6cii; Figure S15, Supporting Information) and high cell viability of 98.83 ± 0.95% via Propidium iodide analysis; Equation (5) (Figure 6ciii; Figure S16, Supporting Information). However, the HDFs cultured on the 0.50 and 0.75 hydrogels registered a significant decrease in metabolic activity by day 7, suggesting that the HDFs were less viable. This cytotoxic effect was likely due to the higher amount of Ag present in the 0.50 and 0.75 hydrogels compared to the 1.00 and 1.25 hydrogels. Although the 1.00 hydrogel performed better than that of 0.50 and 0.75 as a template for the culture of HDFs, their cell viability dropped from 91.86 ± 2.75% on day 1 to 78.97 ± 6.36% by day 7. These results demonstrated the compatibility of the hydrogels to support cell proliferation in relation to the thiol:Ag mole ratio, in which the 1.25 hydrogel was demonstrated to be the best.

Besides assessing the ability of a substrate to support cell proliferation, information on their adhesion, morphology and spreading is crucial. HDFs cultured on the 1.25 hydrogel were

spherical on day 1 of culture, after which a portion of the cells elongated to exhibit the typical spindle-like morphology (day 3) of healthy cells. While healthy cell morphology was not as readily present on the HHK hydrogels in the early timepoints of culture when compared to the collagen controls, it became the dominant morphology by day 7 (Figure 6d).

2.8. HDFs Cultured on Ag-based Hydrogel Do Not Experience Elevated Oxidative Stress

In wound healing, reactive oxygen species (ROS) are a double-edged sword, and when present in persistently high levels, they impose cell injuries and can lead to chronic inflammation and wound repair impairment.[52] The Ag^+ mechanism of action against bacteria is commonly postulated to be the disruption of bacterial membranes and oxidative stress.[53,54] Thus, it is important to ensure that the antibacterial 1.25 hydrogel does not induce sustained ROS production in the HDFs. This was evaluated with the CellROX green reagent, which oxidizes in the presence of ROS into a photostable bright green fluorophore and binds to DNA (Figure S17, Supporting Information). On day 1, the integrated intensity of CellROX green per cell was measured to be significantly higher for the 1.25 hydrogel than the control. However, the intensities decreased from day 3 onward and were at levels lower than the control (Figure 6e). Integrin-mediated cell adhesion and spreading of fibroblasts have been reported to induce ROS production transiently.[55] Poor cell adhesion on Day 1 of culture, as reflected by the spherical cell morphology on the 1.25 hydrogel, would have induced ROS generation, which in turn facilitated improved cell spreading as seen in the later timepoints (Day 3 and 7). Nonetheless, ROS production at all timepoints for the 1.25 hydrogel and control was significantly lower than in the 200 µM tert-Butyl hydroperoxide (tBHP) treated positive control (Figure S18, Supporting Information) and therefore, the concern of oxidative stress generation due to substrate cytocompatibility is not significant.

2.9. The HHK-Ag Gradient Hydrogel Supports HDFs in ECM Production and Alpha-smooth Muscle Actin (α-SMA) Expression

Biosynthesis of ECM by HDFs cultured in the 1.25 hydrogel was assessed using immunofluorescence to locate fibronectin (FN) and collagen type III. FN is an adhesive glycoprotein present in the ECM, which possesses binding domains for integrins and participates in all four stages of wound healing.[56] Here, HDFs cultured on the 1.25 hydrogel had higher expression of FN compared to the control at day 7 (**Figure 7a**). Since collagen III deposition is regulated by FN,[57] the 1.25 hydrogel supported the HDFs in expressing higher levels of collagen III than the control as well (Figure 7b). This outcome is favorable as the expression of collagen III plays an important role in the formation of the granulation tissue during the proliferation phase of wound healing.[58] Wound closure is often reported to be contributed by myofibroblasts, which express α-SMA, and for tissue regeneration substrates, one common activator for the fibroblast-to-myofibroblast transition is the substrate stiffness-induced mechanotransduction.[59] However, for both the control and 1.25 hydrogel, their respective compressive modulus of 1.02 ± 0.11 and 1.04 ± 0.18 kPa (Data not shown) are classified as soft hydrogels.[60] Yet, the HDFs cultured on the 1.25 hydrogel expressed α-SMA significantly, at levels higher than the control. (Figure 7c) One possibility, as reported numerously by others, is the presence of Ag-based materials such as Ag nanoparticles, that induced α-SMA expression in vitro[61] and in vivo, leading to a larger extent of reepithelialization in a murine model.[62] Although the mechanism of action for this phenomenon is not reported, the corroboration of our results with these published work suggests the potential of the 1.25 hydrogel in accelerating wound closure in vivo.

With cytocompatibility of the 1.25 hydrogel toward HDFs shown, the potential cytotoxicity of the substrate toward keratinocytes was next investigated. Immortalized human epidermal keratinocytes (KerCT) at two densities; 10 and 20k cells cm^{-2}, were treated with increasing $AgNO_3$ concentrations. For both, the CC_{50} could not be determined. KerCT seeded at 10k cells cm^{-2} decreased in normalized metabolic activity when treated with 50 µM $AgNO_3$ and lost their polygonal morphology, in a similar way to the KerCT treated with tBHP (Figure S19a, Supporting Information). When the KerCT seeding density doubled, their morphologies were independent of the treatment concentrations, and no decrease in metabolic activity was recorded (Figure S19b,c, Supporting Information). This was expected with an increased cell density but a constant absolute amount of Ag^+. The amount of Ag^+ per cell decreases, thus reducing the cytotoxic pressure of Ag^+.[63] These results reflected a possible decreased toxic effect of Ag^+ in a wound-healing context where cell densities increase across the healing process. Altogether, the antibacterial 1.25 hydrogel supportive of HDF proliferation, ECM production, α-SMA expression, and KerCT viability, corroborates the potential use of this gradient dermal template for skin regeneration (Figure 4c).

2.10. HHK-Ag Gradient Hydrogels Support Active Healing of Full-thickness Wounds In Vivo

To verify the wound healing efficacy of the 1.25 hydrogel, a full-thickness wound model in a mouse was adopted. For this purpose, the 1.25 hydrogel was flipped such that the porous surface of the hydrogel faced the wound bed and the nonporous surface containing higher Ag concentration faced outward (Figure 4c). Gelatin methacrylate (GelMA) hydrogel was selected as the 3D hydrogel control for its widespread use as reported.[64] As the 1.25 hydrogels were not transparent, wound beds could not be observed visually and appeared to heal more slowly than other treatment groups (Figure S20a, Supporting Information). Also, despite daily monitoring and reapplication of the Tegaderm, some of the hydrogels fell out along with the Tegaderm before the stipulated timepoints (Table S4, Supporting Information). Hence, assessing the effectiveness of the treatment groups through wound size measurements was deemed inaccurate, and histological analyses of the tissue sections were adopted instead (**Figure 8**).

More neutrophil recruitment was observed for the 1.25 hydrogel on day 4 (black arrows in Figure 8ci,ei). In addition, the epithelial tongue was seen to migrate under the 1.25 hydrogel more than the GelMA hydrogel (Figure 8d-i,f-i). Regardless, both the GelMA and 1.25 hydrogels did not elicit

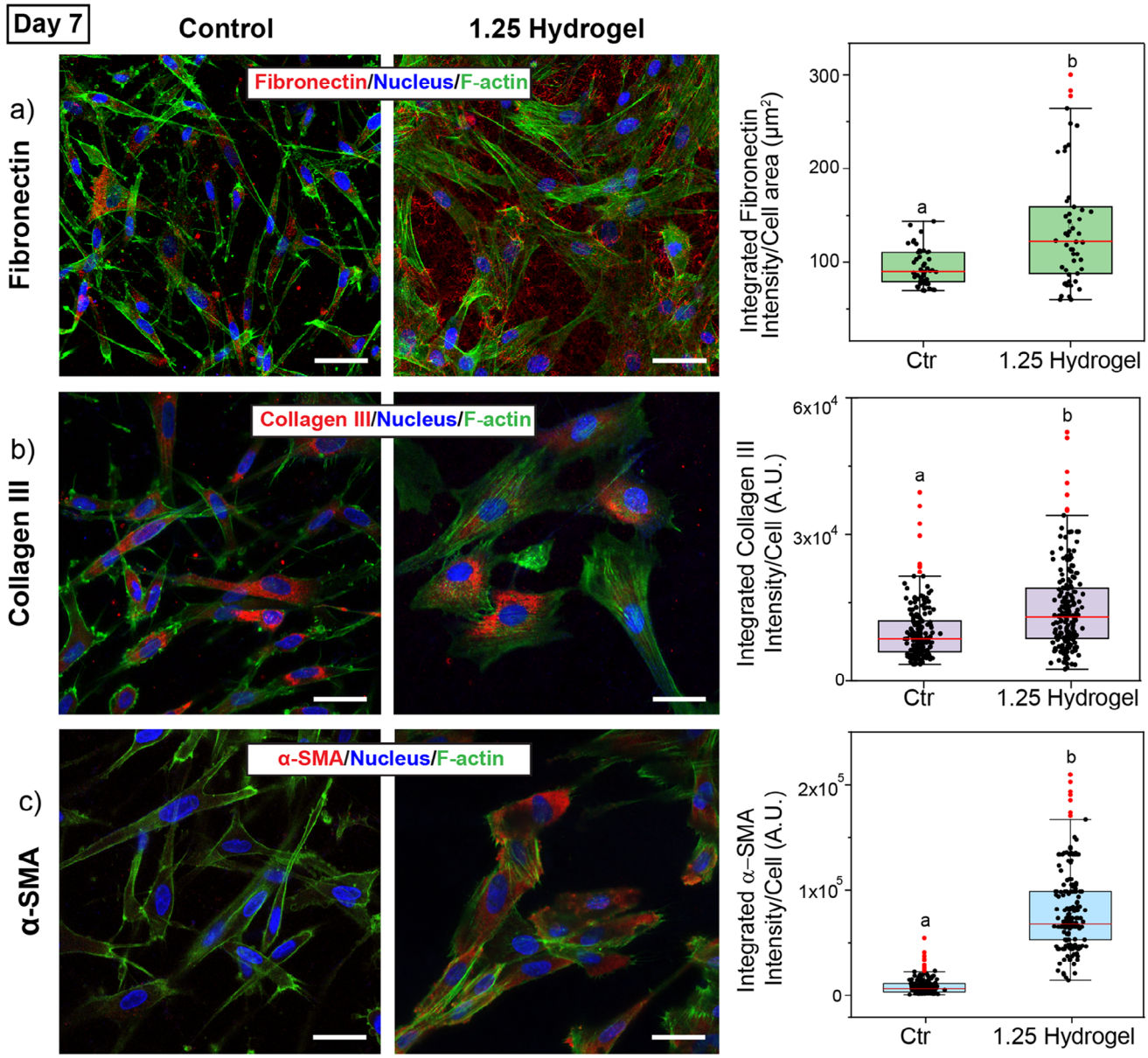

Figure 7. The 1.25 hydrogel supports the cultured HDFs in the biosynthesis of a) fibronectin and b) collagen type III at levels higher than the control hydrogel. c) HDFs cultured on the 1.25 hydrogel express more α-SMA than the control. Scale bar: 50 μm. For all boxplots, the minimum and maximum boundary lines represent the 25th and 75th percentile values, respectively. The median value is presented by the red line. Both top and bottom whiskers represent the 1.5SD limits, and outliers in red were excluded from the statistical analysis (n = 200). All quantitative data are represented as means ± SD. Samples labeled with different letters are statistically different at $< p$ 0.05; Two-tailed Student's *t*-test.

excessive host tissue response. Also, exposure of the wound bed to the 1.25 hydrogel at the initial days might have elicited a lasting wound healing effect on the timepoints of day 4 and 7. This is evident in the histological analyses of the tissue sections where wounds treated with the 1.25 hydrogels had greater epithelial tongue length than the GelMA hydrogels (755.51 ± 391.40 vs 412.04 ± 181.15 μm; $p < 0.05$) by day 7 (Figure 8g). 25% of wounds treated with the control and 1.25 hydrogel could achieve complete reepithelialization by the end of the study (Figure S20 b–f, Supporting Information). As discussed in the in vitro studies, the presence of Ag could have played a role in facilitating greater reepithelialization.[62] In contrast, none of the GelMA hydrogel-treated wounds reepithelialized completely.

Collagen, one of the basic components in the dermis ECM, is key for wound healing.[64] The extent of collagen deposition and ECM remodeling at the wound sites was assessed with picrosirius red (PSR) staining. Positive PSR signals were observed in the wound beds for all groups on day 7 (Figure 8h–j). Granulation tissue formed in the wounds treated with the 1.25 hydrogel expressed the highest collagen content, that was 1.95 times and 1.42 times of that in the control and in GelMA, respectively (Figure 8k). This is in agreement with the in vitro study where

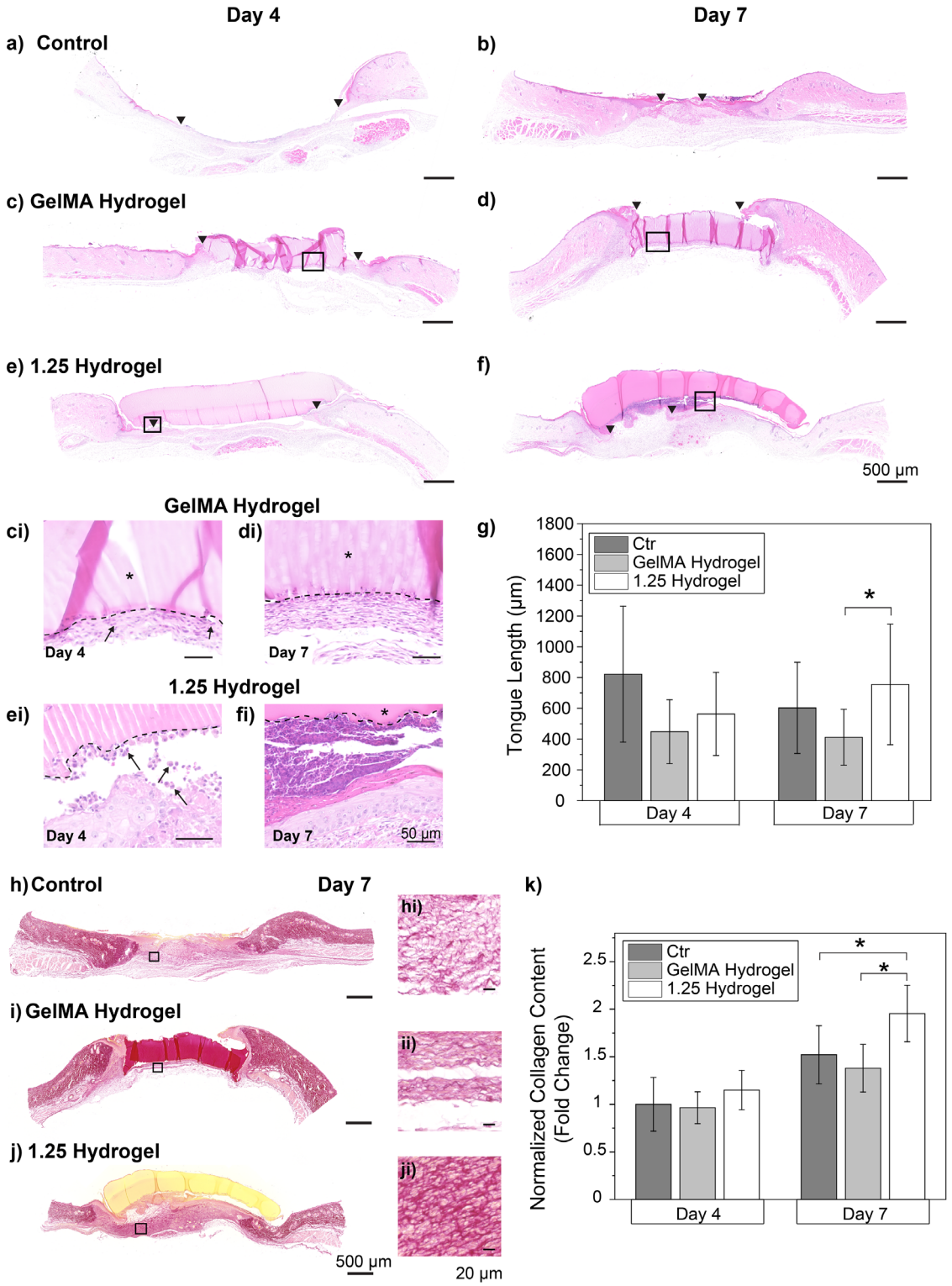

Figure 8. Wounds treated with the 1.25 hydrogel resulted in faster reepithelialization than GelMA hydrogel and produced the most collagen by day 7. Representative H&E-stained tissue sections at day 4 and day 7 for the a,b) control, c,d) GelMA hydrogel, and e,f) 1.25 hydrogel. Black triangles demarcate the wound boundaries, showing the length of the epithelial tongue. Black squares indicate the region of interest (ROI) shown in the magnified H&E images of the sample-host tissue interface for the (c-i,d-i) GelMA and (e-i,f-i) 1.25 hydrogel at day 4 and 7, respectively. Asterisks (*), dashed lines, and black arrows indicate the sample, sample-tissue interface, and neutrophils, respectively. g) Quantified epithelial tongue length for all 3 materials at day 4 and 7 (n = 24 for all groups at day 4, n = 26 for control, n = 44 for GelMA hydrogel, and n = 34 for 1.25 hydrogel at day 7). Representative PSR stained tissue sections at day 7 and their magnified images at ROI indicated by the black squares for h,h-i) control, i, ii) GelMA hydrogel, and j,j-i) 1.25 hydrogel.

HDFs seeded onto the 1.25 hydrogel recorded higher levels of collagen production than the control (Figure 7b). Besides collagen production, angiogenesis at the wound site is crucial in clearing metabolic products and facilitating nutrient and oxygen transport.[65] Indeed, blood vessels were evident in the granulation tissue of wounds treated with the 1.25 hydrogel and in the control, indicating neovascularization (Figure S21, Supporting Information).

3. Conclusion

A gradient hydrogel based on cross-linking of HHKs using Ag^+ was developed. This gradient hydrogel was fabricated using a facile method unique to HHKs, via Ag—S complexation achieved by simple diffusion of Ag^+ through a HHK solution. Due to instantaneous formation of Ag—S complexation, the use of an external partially permeable membrane, which is typically required for diffusion-based gelation, was not required here. The diffusion kinetics of Ag^+ can be modulated by varying the mole ratio of free thiols in HHK to $Ag^{+,}$ which in turn affects the rate of gelation. As the thiol:Ag ratio decreased from 1.25 to 0.50, the initial Ag^+ concentration increased, and the rate of gelation increased from 0.12 ± 0.05 to $1.55 \pm 0.23 \times 10^{-5}$ cm^2 s^{-1}. This shortened the gelation time from 12.92 ± 0.52 to 4.92 ± 0.29 h. Interestingly, a porosity gradient could be formed in a single step, and this gradient microstructure is controllable with the thiol:Ag mole ratio. Moreover, these pores displayed a nonuniform wall thickness, which ranges from 0.35 ± 0.11 to 6.09 ± 1.96 µm. The correlation between the tunable gradient microstructure and hydrogel properties was manifested in the mechanical properties, degradation profiles, and water uptake capacity. The gradient hydrogel with distinctively different topographies at the top and bottom surfaces suggested a possible notion of using this system as a dermal template for skin regeneration. At a balanced thiol:Ag ratio of 1.25, the hydrogel was found to be antibacterial against *Staphylococcus aureus* and supported the attachment, spreading, and proliferation of HDFs. Also, it supported the HDFs in ECM production and expression of α-SMA. Furthermore, when employed as a dermal template in a full-thickness excisional wound model, the 1.25 hydrogel promoted the most collagen production by day 7 and greater reepithelialization than the 3D GelMA hydrogel. Notably, the upcycled HHK gradient hydrogel did not elicit a significant host tissue response. This work has validated the feasibility of HHKs, a natural biomaterial, to be repurposed into a functional gradient hydrogel for wound healing and tissue regeneration.

4. Experimental Section

Extraction of Human Hair Keratins: Random human hair waste was retrieved from local salons, and keratins were extracted using a two-step reductive Shindai method.[66] First, the hair was cleansed with soap and subsequently rinsed thoroughly with 70% ethanol (1.00983, Sigma–Aldrich). Post-drying, the hair samples were delipidized through immersion in a mixture of chloroform (132 950, ReagentPlus) and methanol (A412-500, Thermo Fisher) for 24 h, and once dried, the hair was cut into short fragments. To dissociate the KAPs, the fragments were added into a 25 mM Tris HCL (T1503, Sigma–Aldrich) buffer solution at pH 9.5, comprising 8 M urea (U5378, Sigma–Aldrich), 200 mM dithiothreitol (DTT10, Gold Bio), 25% ethanol at 50 mg mL^{-1} for 72 h at 50 °C. The resultant suspension was filtered, and the residual KAP-free hair was washed with deionized (DI) water and left to air-dry. Next, HHKs were extracted from KAP-free hair soaked into a 25 mM Tris-HCL buffer solution at pH 8.5, comprising 2.6 M thiourea (T7875, Sigma–Aldrich), 5 M Urea, 200 mM DTT at 50 mg mL^{-1} for 24 h at 50 °C. The HHK extracts were filtered, and the filtrate was transferred into a 10K MWCO dialysis tubing (88 245, Thermo Fisher) and dialyzed against DI water until the pH of the extracts reached 6.5. The protein and free thiol concentration of the dialyzed HHKs were quantified using the Pierce bicinchoninic acid assay kit (23 225, Thermo Fisher) and Ellman's assay (22 582, Thermo Fisher) according to the manufacturer's protocol.

TEM: The samples were prepared based on an established protocol.[21] Briefly, samples at 0.4 mg mL^{-1} were drop-cast onto a glow-discharged full carbon-coated TEM grid (0 1821, Ted Pella). To remove excess solution, a filter paper was used to blot the grid. This was followed by washing with DI water and blotting. Last, the sample was stained negatively with 2% uranyl acetate and blotted. The grid was left to dry and kept overnight in a dry box before viewing under the TEM (2010 UHR, JEOL). Image analysis was conducted using ImageJ.

HHK-Ag Gradient Hydrogel Formation: The dialyzed HHK solution was diluted to 30 mg mL^{-1}, and concentrations of silver nitrate ($AgNO_3$) required for the 5 thiol:Ag ratios were prepared based on the free thiol g^{-1} of HHK obtained (Table S1, Supporting Information). The hydrogels were prepared in individual wells of a 24 well plate, and for each hydrogel, 1 mL of HHK solution and 1 mL of $AgNO_3$ solution were utilized. To create the thin gel layer as the partially permeable membrane (PPM), small amounts of the HHK solution were dropped cast onto the 1 mL of $AgNO_3$ (Video S1, Supporting Information). After PPM formation, the remaining HHK were added, and the diffusion-mediated gelation was conducted overnight for 16 h. The formed hydrogels were removed from the well plate and washed 3 times with DI water to remove excess Ag^+ prior to subsequent characterization analyses.

Quantification of Silver Concentration: Silver ion concentrations were quantified using an Inductively Coupled Plasma Optical Emission Spectrometer (ICP-OES) (Optima 8000, Perkin Elmer). Before analysis, all samples were diluted and acidified to pH 1–2 with 1% nitric acid. A syringe filter (0.45 µm) was used to filter each sample. 3 mL of the test sample was introduced at a flow rate of 1.5 mL min^{-1} into the plasma chamber. Samples were analyzed in axial mode, with the emission line of Ag at 328.068 nm. The concentration of each sample was determined by comparing the emission intensity against that of the silver standard for ICP (12 818, Sigma–Aldrich).

Turbiscan Lab Analysis: The gelation kinetics were quantified using the Turbiscan Lab Analyzer (Microtrac MRB). The hydrogel was fabricated in a 15 × 45 mm clear glass screw thread vial and placed into the sample chamber. The transmittance and backscatter of the near-infrared light passed through the sample vial were measured along the sample height every 40 µm for 16 h at 15-min intervals as the keratin solution gels. The data obtained were exported into Excel for analysis. The time required for complete gelation was taken as the time when a decrease in transmittance was no longer observed. The apparent diffusion coefficient of the gel front (D_{app}) was measured using the following equation, where d is the gel thickness in cm and t is the time in seconds at which the gel thickness is taken.

$$d^2 = 2D_{app}t \quad (1)$$

k) Quantified normalized collagen content for all 3 materials at day 4 and 7 (n = 6 for all groups at day 4, n = 11 for control, and n = 12 for GelMA and 1.25 hydrogels at day 7). All quantitative data are presented as means ± SD, * $p < 0.05$; One-way Welch ANOVA with Games–Howell post-hoc test was adopted.

X-Ray Photoelectron Spectroscopy (XPS): The XPS analysis was performed with the AXIS Supra spectrometer (Kratos Analytical) fitted with a monochromatic Al K-alpha source (1487 eV) operated at 15 kV and 15 mA and a hemispherical analyzer. All samples were lyophilized and stored in a dry box before measurement. Charge build-up on the sample surface was neutralized by a 3.1-volt bias. Wide scans and narrow scans were recorded at 160 and 20 eV pass energy, respectively. All spectra were processed and analyzed with the ESCApe software, and charge correction of the binding energies was done against the carbon 1 s at 284.4 eV.

Inhibition of Free Thiols: The blocking of thiols with N-ethylmaleimide (NEM) (23 030, Sigma–Aldrich) was carried out on the same day after the completion of HHK to minimize the disulfide bond formation. After quantifying the concentration of free thiols in HHKs post-dialysis, a 10-molar excess amount of NEM was reacted with HHKs for 2 h at room temperature. Following, the NEM–HHK solution was dialyzed against DI water to remove unreacted NEM overnight. Ellman's assay was conducted on the NEM–HHK solution to verify the successful blocking of free thiols.

SEM: To view the hydrogels' surface topographies, the samples were lyophilized and sliced into smaller pieces for sample preparation. For viewing of the cross-sectional microarchitecture of the hydrogels, they were flash-frozen in liquid nitrogen for 5 min and immediately sliced into half to expose the cross-section before lyophilization. The samples were then gold-coated for 30 s and viewed under the thermionic SEM (JSM-6360, JEOL) at an accelerating voltage of 10 kV and spot size of 50.

Oscillatory Amplitude Sweep Test: The storage and loss modulus of the gradient hydrogels were characterized through an oscillatory amplitude sweep using a rheometer (MCR 501, Anton Paar) accessorized with a 10 mm parallel plate spindle (PP10, Anton Paar). The normal force of 0.02–0.05 N was maintained during the measurements. The amplitude sweep test was conducted between 0.01 and 1000% strain at a constant frequency of 6.28 rad s^{-1}. The tests were conducted with the top surface of the hydrogel in contact with the plate spindle.

Uniaxial Compression Test: The hydrogels were subjected to uniaxial compression using an electromechanical test (Criterion Model 42, MTS) equipped with a 250 N load cell. Hydrogels of 15 mm diameter and 5 mm height were placed between two platens and pre-loaded with 0.02–0.05 N. The hydrogels were compressed at a rate of 0.01 mm s^{-1} up to 80% strain. Compressive modulus was taken as the secant modulus obtained at 10% strain from the linear region of the stress–strain slope. Compressive strength was recorded as the highest stress that each sample could withstand. The tests were conducted with the top surface of the hydrogel in contact with the top platen.

In vitro Degradation Test: Each hydrogel was placed onto a cell strainer insert of pore size 40 µm (93 040, SPL Life Sciences) that sits nicely in a 6-well plate. 10 mL of ProK (P2308, Sigma–Aldrich) solution at 0.5 U mL^{-1} was added into each well to ensure full submersion of the hydrogel. The samples (n = 6) were then placed into a 37 °C oven with a shaking platform (180 rpm), and at each timepoint, the hydrogels were removed from the oven and rinsed with DI water to remove any PBS salts. Following, they were lyophilized, and their dry weight was measured ($W_{timepoint}$). The average of 6 lyophilized pristine hydrogels was taken as the original dry weight ($W_{original}$) of each parameter. The remaining mass was calculated using the following equation

$$\text{Remaining mass}\ (\%) = \frac{W_{timepoint}}{W_{original}} \times 100\% \quad (2)$$

Water Uptake: The hydrogel samples were lyophilized to form scaffolds for this study. They were kept in a dry box right until the day of the study, and their dry weight was recorded as $W_{original}$. Each scaffold was placed in a well of a 24-well plate, and 2 mL of DI water was added to each well. The plate was kept overnight at 37 °C, and the following day, the scaffolds were removed from the well, and excess water was wiped off from the scaffolds using wax paper. The weight of the hydrated scaffold was recorded as W_{wet} and the water uptake percentage was calculated using the following equation

$$\text{Water Uptake}\ (\%) = \frac{W_{wet} - W_{original}}{W_{original}} \times 100\% \quad (3)$$

Kirby–Bauer Disk Diffusion Susceptibility Test: The protocol was adopted from the Kirby–Bauer disk diffusion susceptibility test protocol.[67] Antibacterial properties of the HHK-Ag gradient hydrogels (0.50 and 1.25 thiol:Ag ratio) were tested against Gram-positive *Staphylococcus Aureus* (25 923, ATCC). LB agar plates were prepared by dissolving Luria–Bertani (LB) agar powder (244 520, BD) into DI water at 4% and casting it into 100 mm Petri dishes after autoclaving. The strain was subcultured in LB broth (244 620, BD) under constant shaking at 37 °C for 18 h to the mid-exponential phase. The bacterial suspension was adjusted to the 0.50 McFarland standard, and 150 µL was added to the LB agar plate and swabbed evenly for inoculation. All hydrogels were washed with DI water to remove excess unbound Ag^+ before the testing. HHK solution was used as a negative control. 20 µL of the solution was loaded onto the disc (12 mm), and hydrogel samples (12 mm) were placed onto an unloaded disc. The discs were transferred onto the plates and were incubated at 37 °C for 24 h and subsequently imaged using the iBright Imaging system (CL1000, Thermofisher). The zones of inhibition were measured using ImageJ.

Cell Culture: Human dermal fibroblasts (PCS-201-012, ATCC) were cultured in Dulbecco's Modified Eagle Medium (DMEM) (12 800 017, Gibco) supplemented with 10% fetal bovine serum (FBS) (SV30160, GE Healthcare) and 1% penicillin–streptomycin (15 140 122, Gibco). Immortalized human epidermal keratinocytes, KerCT (CRL-4048, ATCC) were cultured in supplemented EpiGRO media (SCMK001, Merck Millipore). EpiGRO was supplemented with the supplement kit provided by the supplier. Both cell types were cultured at 37 °C, 5% CO_2, and 95% humidity with media changes every two days until they have reached a confluency of 80%. Before seeding onto hydrogel samples or well plates, cells adhered to the cell culture flask were removed by trypsinization, and cell counting was conducted with a hemocytometer. HDFs of passage numbers 5–8 were used for cell culture studies. For all studies, cells were seeded at a density of 10 000 cells cm^{-2} unless stated otherwise. The control type I bovine collagen hydrogel was fabricated as per the manufacturer's instructions (5005, Advanced Biomatrix). The cells were seeded on the top surface of the gradient hydrogel only. For all confocal imaging conducted on the processed hydrogel samples, the sample was flipped to face the seeded surface (Top) down onto the coverslip. The loaded coverslip was then placed onto the stage of the confocal laser scanning microscope.

Leaching Study: Before the leaching studies, all hydrogels were washed thrice with sterile PBS to remove unbound excess Ag^+ and equilibrated in DMEM overnight. The day after was deemed day 0, and at each timepoint (days 1, 3, 5, and 7) the media was collected for analysis, and fresh media was added to continue toward the next timepoint. The collected samples were diluted with 1% nitric acid and syringe filtered (0.45 µm) to remove any particulates. The concentration of Ag^+ was quantified with ICP-OES. Cumulative release was calculated using the equation below. For the leaching study in the presence of HDFs, the same procedure was carried out, with the additional seeding step onto the hydrogel surface at 10 000 cells cm^{-2} at day 0.

$$Ag^+\ (\%) = \frac{\text{Concentration}\ \left(\frac{mg}{L}\right) \times \text{Leaching Volume}\ (L)}{\text{Amount of}\ Ag^+\ \text{added to hydrogel}\ (mg)} \quad (4)$$

Metabolic Assay and Cell Viability: Metabolic activity of the cultured cells was assessed with the Alamar Blue assay (A50101, Thermo Fisher). At each timepoint, the media was aspirated from each sample, and fresh media containing the reagent was added according to the manufacturer's instructions. The samples were placed in the incubator for 3 h, and metabolic activity was recorded as the fluorescence intensity emitted at 590 nm (Biotek Synergy H1, Agilent). Cell viability of the cultured cells was evaluated using the Hoechst 33 342 to stain all nuclei and Propidium

iodide (PI) (P4864, Thermo Fisher) to stain for dead cells at a dilution of 1:10 000 and 1:1000 in PBS, respectively. After staining was completed, the samples were viewed under a confocal laser scanning microscope (LSM 710, Carl Zeiss). The images were analyzed using the Analyze Particle function in ImageJ. Cell viability was calculated using the following equation

$$\textit{Cell viability}\ (\%) = \left(\frac{\textit{Total number of cells} - \textit{Number of PI stained cells}}{\textit{Total number of cells}}\right) \times 100\% \quad (5)$$

CellROX Green Oxidative Stress: To detect and quantify the presence of oxidative stress in the HDFs cultured on the samples, the CellROX Green reagent (C10444, Thermo Fisher) was added to the live cells at each timepoint according to the manufacturer's protocol. All nuclei were stained with Hoechst 33 342. HDFs cultured on glass coverslips treated with 200 µM tBHP for 2 h were taken as the positive control. After staining, images of the samples were captured with under a confocal laser scanning microscope (Stellaris 5, Leica). The integrated CellROX Green intensity per cell was quantified using the threshold function in ImageJ

Immunofluorescence (IF) Staining: IF staining of the hydrogels was conducted independently against fibronectin (ab2413, Abcam) collagen III (ab7778, Abcam), and alpha-smooth muscle actin (ab7817, Abcam). On day 7, the HDF-cultured hydrogels were washed with chilled PBS and fixed with 4% paraformaldehyde (PFA) (P6148, Sigma–Aldrich) for 20 min. 0.2% Triton X-100 (X-100, Sigma–Aldrich) in PBS was used to permeabilize the cells, and the samples were blocked with 2% BSA (A3733, Sigma–Aldrich) in PBS for one hour. Next, the samples were incubated with the primary antibodies diluted in 0.2% BSA and 0.1% Triton X-100 in PBS overnight at 4 °C. Thereafter, samples were washed with PBS to remove unbounded primary antibodies and the appropriate secondary antibodies (A21443/A21463, Thermo Fisher) together with Hoechst 33 342 for nucleus staining and phalloidin 488 (A12379, Thermo Fisher) for actin filament staining was added at room temperature for 1 h. After staining was completed, the samples were viewed under a confocal laser scanning microscope (Stellaris 5, Leica). Images taken were analyzed respectively using ImageJ, where fluorescence intensity was quantified with the threshold function by integrated intensity.

In Vivo Wound Healing Study: The full-thickness excisional mouse model was approved by the Institutional Animal Care and Use Committee (IACUC) in Nanyang Technological University, Singapore, and conducted in adherence to the National Advisory Committee for Laboratory Animal Research (NACLAR) guidelines. This model was used to evaluate the effectiveness of the 1.25 HHK-Ag gradient hydrogel as a dermal template for wound healing. A total of 3 sample groups were tested: control (no intervention), gelatin methacrylate (GelMA) hydrogel (3D control), and 1.25 hydrogel. All hydrogel samples were fabricated, sterilized, and punched to a diameter of 6 mm prior to implantation. Each C57BL/6J mouse was anesthetized through isoflurane inhalation. After shaving, a 6 mm biopsy punch (Paramount) was used to create two identical and symmetrical full-thickness excisional wounds were made on the sterilized dorsal skin along the posterior midline on each mice. The samples were implanted randomly onto each wound while ensuring that no groups were repeated in a single mouse. For the 1.25 hydrogel, the hydrogel was flipped so that the top porous surface of the hydrogel (Figure 4c) was facing downward into the wound. Tegaderm was applied to protect the wounds and keep the hydrogels in place. For the day 4 timepoint, there were a total of 6 and 12 wounds/group for day 7. On days 4 and 7, the mice were euthanized, and the dorsal skins were excised and fixed in 4% PFA overnight at 4 °C for processing. Briefly, sterile GelMA (SKU0010, Gelomics) and LAP photoinitiator (VL-LP0000, CELLINK) were mixed to reach a final concentration of 10% and 0.2% respectively. The pre-polymer solution was crosslinked at 405 nm with the LunaCross-linker (SKU0004, Gelomics) for 90 s. The hydrogels were then punched to a diameter of 6 mm prior to implantation.

Histological Analysis: The fixed tissues were bisected, dehydrated, and embedded in paraffin. The tissues were sectioned to 5 µm thickness using a microtome (RM2265, Leica). Hematoxylin and Eosin (H&E) staining was conducted to visualize tissue morphology. The tissues were deparaffinized on a heat plate and hydrated with 3 changes of xylene, followed by descending absolute ethanol concentrations (100%, 90%, 80%, 70%) and tap water, at an interval of 3 min each. The hydrated tissues were stained in the hematoxylin dye for 5 min and washed in running tap water for 30 s. Next, the tissues were submerged in acid alcohol for 15 s, followed by Scott's tap water for 2 min and eosin dye (2 min), with washing between each step. The stained tissue sections were dehydrated in ascending absolute ethanol concentrations (70%, 80%, 90%, 100%) followed by 3 xylene changes. They were mounted with CytoSeal 60 (Electron Microscopy Studies). Picrosirius Red Staining (PSR) was conducted according to the manufacturer's protocol to visualize collagen fibers within the tissues (ab150681, Abcam). Briefly, the deparaffinized tissues were hydrated. PSR staining was conducted for one hour at room temperature. The stained tissues were quickly rinsed in two changes of 0.5% acetic acid solution, followed by a rinse in absolute ethanol. Finally, the tissues were dehydrated in two changes of absolute alcohol, followed by xylene and mounted. Brightfield images of the histological sections were captured with a slide scanner (AxioScan, Zeiss). Collagen deposition and epithelial tongue length measurements were conducted in ImageJ. The measured collagen content in the granulation tissues was normalized against the collagen content in the normal skin area of the same tissue section.

Statistical Analysis: All experiments were conducted with a minimum of three technical, biological, or extraction replicates, and the number of samples (n) for each study is indicated in their respective figure captions. All quantitative data are presented as mean ± standard deviation (SD). For comparison between two sample groups, a two-tailed Student's *t*-test was conducted in Microsoft Excel. For comparison between more than two sample groups with equal variance, a one-way analysis of variance (ANOVA) with Tukey's honestly significant difference (HSD) post-hoc test was conducted with the Origin 2020 software. For non-equal variance, one-way Welch ANOVA with Games–Howell post-hoc test was conducted with the Origin 2020 software. Differences between two sample groups were considered statistically significant when $p < 0.05$.

Supporting Information

Supporting Information is available from the Wiley Online Library or from the author.

Acknowledgements

This work was supported by the Ministry of Education, Singapore (AcRF Tier 1: RG7/22 & RT04/20) and the NTUitive GAP Fund (NGF-2022-12-002). The authors would like to acknowledge support from the Facility for Analysis, Characterization, Testing, and Simulation (FACTS), Nanyang Technological University, Singapore, for SEM, TEM, and XPS evaluation. Also, the authors would like to acknowledge Dr Teddy Salim from FACTs, for his assistance in XPS analysis, and Ms Koh Dan Yu from NEWRI Analytics Cluster, Nanyang Technological University, Singapore, for the guidance in operating ICP-OES. The authors would like to thank Ms Khoo Ee Von for creating the illustrations in the manuscript.

Conflict of Interest

The authors declare no conflict of interest.

Data Availability Statement

The data that support the findings of this study are available in the supplementary material of this article.

Keywords

antibacterial, gradient hydrogel, human hair keratins, metal-thiolate complexation, tissue engineering

Received: August 12, 2025
Revised: September 16, 2025
Published online: November 7, 2025

[1] V. Singh, S. Wang, K. W. Ng, In *Comprehensive Biomaterials II*, (Ed. P Ducheyne), Elsevier, Oxford **2017**, pp. 542–557.
[2] S. Wang, F. Taraballi, L. P. Tan, K. W. Ng, *Cell Tissue Res.* **2012**, *347*, 795.
[3] S. Z. Wang, S. E. Wang, M. Foo, N. S. Tan, Y. Yuan, W. Lin, Z. Zhang, K. W. Ng, *ACS Appl. Mater. Interfaces* **2015**, *7*, 5187.
[4] K. Yue, Y. Liu, B. Byambaa, V. Singh, W. Liu, X. Li, Y. Sun, Y. S. Zhang, A. Tamayol, P. Zhang, K. W. Ng, N. Annabi, A. Khademhosseini, *Bioeng. Transl. Med.* **2018**, *3*, 37.
[5] H. J. Kang, N. Ko, S. J. Oh, S. Y. An, Y.-S. Hwang, S. Y. Kim, *Int. J. Mol. Sci.* **2021**, *22*, 13269.
[6] B. Y. Tan, L. T. H. Nguyen, K. W. Ng, *Mater. Today Commun.* **2022**, *30*, 103049.
[7] H. Lee, K. Noh, S. C. Lee, I.-K. Kwon, D.-W. Han, I.-S. Lee, Y.-S. Hwang, *Tissue Eng. Regener. Med.* **2014**, *11*, 255.
[8] H. Y. Lai, S. Wang, V. Singh, L. T. H. Nguyen, K. W. Ng, *J. Biomater. Sci. Polymer Ed.* **2018**, *29*, 1081.
[9] H. M. Chua, Z. Zhao, K. W. Ng, *Macromol. Rapid Commun.* **2020**, *41*, 2000254.
[10] P. Hartrianti, L. T. H. Nguyen, J. Johanes, S. M. Chou, P. Zhu, N. S. Tan, M. B. Y. Tang, K. W. Ng, *J. Tissue Eng. Regener. Med.* **2017**, *11*, 2590.
[11] Z. K. Moay, L. T. H. Nguyen, P. Hartrianti, D. P. Lunny, D. Leavesley, Y. O. Kok, S. J. Chong, A. W. C. Chua, S.-I. Tee, K. W. Ng, *Int. J. Mol. Sci.* **2021**, *22*, 8594.
[12] P. Casuso, I. Odriozola, A. Pérez-San Vicente, I. Loinaz, G. Cabañero, H.-J. Grande, D. Dupin, *Biomacromolecules* **2015**, *16*, 3552.
[13] H. Chen, R. Cheng, X. Zhao, Y. Zhang, A. Tam, Y. Yan, H. Shen, Y. S. Zhang, J. Qi, Y. Feng, L. Liu, G. Pan, W. Cui, L. Deng, *NPG Asia Mater* **2019**, *11*, 3.
[14] Z. Chen, Z. Cai, C. Zhu, X. Song, Y. Qin, M. Zhu, T. Zhang, W. Cui, H. Tang, H. Zheng, *Adv. Healthcare Mater.* **2020**, *9*, 2001032.
[15] P. Casuso, A. Pérez-San Vicente, H. Iribar, A. Gutiérrez-Rivera, A. Izeta, I. Loinaz, G. Cabañero, H.-J. Grande, I. Odriozola, D. Dupin, *Chem. Commun.* **2014**, *50*, 15199.
[16] L. Cheng, Z. Cai, T. Ye, X. Yu, Z. Chen, Y. Yan, J. Qi, L. Wang, Z. Liu, W. Cui, L. Deng, *Adv. Funct. Mater.* **2020**, *30*, 2001196.
[17] A. Seidi, M. Ramalingam, I. Elloumi-Hannachi, S. Ostrovidov, A. Khademhosseini, *Acta Biomater.* **2011**, *7*, 1441.
[18] N. Zinkovska, J. Smilek, M. Pekar, *Polymers* **2020**, *12*, 966.
[19] X. Mao, R. Cheng, H. Zhang, J. Bae, L. Cheng, L. Zhang, L. Deng, W. Cui, Y. Zhang, H. A. Santos, X. Sun, *Adv. Sci.* **2019**, *6*, 1801555.
[20] J. Kong, S. Yu, *Acta Biochim. Biophys. Sin.* **2007**, *39*, 549.
[21] H. Y. Lai, M. I. Setyawati, A. R. Ferhan, S. K. Divakarla, H. M. Chua, N.-J. Cho, W. Chrzanowski, K. W. Ng, *ACS Biomater. Sci. Eng.* **2021**, *7*, 83.
[22] J. T. Jacob, P. A. Coulombe, R. Kwan, M. B. Omary, *Cold Spring Harbor Perspect. Biol.* **2018**, *10*, a018275.
[23] R. G. Pearson, *J. Chem. Educ.* **1968**, *45*, 581.
[24] S. Feroz, N. Muhammad, R. Ullah, U. Nishan, P. Cathro, G. Dias, *Front. Bioeng. Biotechnol.* **2023**, *11*, https://doi.org/10.3389/fbioe.2023.1304147.
[25] Y. Wang, R. Xu, G. Luo, Q. Lei, Q. Shu, Z. Yao, H. Li, J. Zhou, J. Tan, S. Yang, R. Zhan, W. He, J. Wu, *Acta Biomater.* **2016**, *30*, 246.
[26] R. A. Franco, Y.-K. Min, H.-M. Yang, B.-T. Lee, *J. Biomater. Appl.* **2013**, *27*, 605.
[27] A. M. Fuentes-Caparrós, Z. Canales-Galarza, M. Barrow, B. Dietrich, J. Läuger, M. Nemeth, E. R. Draper, D. J. Adams, *Biomacromolecules* **2021**, *22*, 1625.
[28] H. Jo, M. Yoon, M. Gajendiran, K. Kim, *Macromol. Biosci.* **2020**, *20*, 1900300.
[29] U. T. D. Huynh, O. Chambin, A. M. du Poset, A. Assifaoui, *Carbohydr. Polym.* **2018**, *190*, 121.
[30] X.-D. Yu, J.-H. Li, H. Li, J. Huang, D. Caccavo, G. Lamberti, L.-Q. Chu, *Int. J. Pharm.* **2021**, *605*, 120804.
[31] C. A. Maestri, P. Bettotti, M. Scarpa, *J. Mater. Chem. B* **2017**, *5*, 8096.
[32] M. T. I. Mredha, X. Zhang, T. Nonoyama, T. Nakajima, T. Kurokawa, Y. Takagi, J. P. Gong, *J. Mater. Chem. B* **2015**, *3*, 7658.
[33] Y. Liu, W. Ma, W. Liu, C. Li, Y. Liu, X. Jiang, Z. Tang, *J. Mater. Chem.* **2011**, *21*, 19214.
[34] X. Cheng, M. Liu, A. Zhang, S. Hu, C. Song, G. Zhang, X. Guo, *Nanoscale* **2015**, *7*, 9738.
[35] M. Zienkiewicz-Strzałka, A. Deryło-Marczewska, R. B. Kozakevych, *Appl. Nanosci.* **2018**, *8*, 1649.
[36] R. C. de Guzman, S. M. Tsuda, M.-T. N. Ton, X. Zhang, A. R. Esker, M. E. Van Dyke, *PLoS One* **2015**, *10*, 0137233.
[37] D. G. Castner, K. Hinds, D. W. Grainger, *Langmuir* **1996**, *12*, 5083.
[38] Z. Liu, J. Du, X. Jin, P. Li, X. Jiang, J. Yuan, *Mater. Lett.* **2019**, *237*, 9.
[39] S. D. Khizhnyak, P. V. Komarov, M. M. Ovchinnikov, L. V. Zherenkova, P. M. Pakhomov, *Soft Matter* **2017**, *13*, 5168.
[40] R. A. Bell, J. R. Kramer, *Environ. Toxicol. Chem.* **1999**, *18*, 9.
[41] B. Holt, A. Tripathi, J. Morgan, *J. Biomech.* **2008**, *41*, 2689.
[42] M. Piejko, K. Radziun, S. Bobis-Wozowicz, A. Waligórska, E. Zimolag, M. Nessler, A. Chrapusta, Z. Madeja, J. Drukala, *Bioengineering* **2020**, *7*, 67.
[43] T.-R. Kim, M.-S. Kim, T. S. Goh, J. S. Lee, Y. H. Kim, S.-Y. Yoon, C.-S. Lee, *Appl. Sci.* **2019**, *9*, 1965.
[44] J. H. Lee, T. G. Park, H. S. Park, D. S. Lee, Y. K. Lee, S. C. Yoon, J.-D. Nam, *Biomaterials* **2003**, *24*, 2773.
[45] X. Zhao, Q. Lang, L. Yildirimer, Z. Y. Lin, W. Cui, N. Annabi, K. W. Ng, M. R. Dokmeci, A. M. Ghaemmaghami, A. Khademhosseini, *Adv. Healthcare Mater.* **2016**, *5*, 108.
[46] N. T.-P. Nguyen, L. V.-H. Nguyen, N. M.-P. Tran, et al., *Mater. Sci. Eng., C* **2019**, *103*, 109670.
[47] K. Odelius, A. Höglund, S. Kumar, M. Hakkarainen, A. K. Ghosh, N. Bhatnagar, A.-C. Albertsson, *Biomacromolecules* **2011**, *12*, 1250.
[48] H. Furukawa, F. Gándara, Y.-B. Zhang, J. Jiang, W. L. Queen, M. R. Hudson, O. M. Yaghi, *J. Am. Chem. Soc.* **2014**, *136*, 4369.
[49] L. J. Bessa, P. Fazii, M. Di Giulio, L. Cellini, *Int. Wound J.* **2015**, *12*, 47.
[50] G. Kallstrom, *J. Clinical Microbiol.* **2014**, *52*, 2753.
[51] G. Mulley, A. T. A. Jenkins, N. R. Waterfield, *PLoS One* **2014**, *9*, 94409.
[52] C. Dunnill, T. Patton, J. Brennan, J. Barrett, M. Dryden, J. Cooke, D. Leaper, N. T. Georgopoulos, *Int. Wound J.* **2017**, *14*, 89.
[53] I. X. Yin, J. Zhang, I. S. Zhao, M. L. Mei, Q. Li, C. H. Chu, *Int. J. Nanomed.* **2020**, *15*, 2555.
[54] T. C. Dakal, A. Kumar, R. S. Majumdar, V. Yadav, *Front. Microbiol.* **2016**, *7*, https://doi.org/10.3389/fmicb.2016.01831.
[55] P. Chiarugi, G. Pani, E. Giannoni, L. Taddei, R. Colavitti, G. Raugei, M. Symons, S. Borrello, T. Galeotti, G. Ramponi, *J. Cell Biol.* **2003**, *161*, 933.
[56] E. A. Lenselink, *Int. Wound J.* **2015**, *12*, 313.
[57] J. Sottile, D. C. Hocking, *Mol. Biol. Cell* **2002**, *13*, 3546.
[58] J. Patten, K. Wang, *Adv. Drug Delivery Rev.* **2021**, *170*, 353.

[59] B. Hinz, *J. Invest. Dermatol.* **2007**, *127*, 526.
[60] X. Huang, N. Yang, V. F. Fiore, T. H. Barker, Y. Sun, S. W. Morris, Q. Ding, V. J. Thannickal, Y. Zhou, *Am. J. Respiratory Cell Molecular Biol.* **2012**, *47*, 340.
[61] C. You, Q. Li, X. Wang, P. Wu, J. K. Ho, R. Jin, L. Zhang, H. Shao, C. Han, *Sci. Rep.* **2017**, *7*, 10489.
[62] X. Liu, P.-Y. Lee, C.-M. Ho, V. C. H. Lui, Y. Chen, C.-M. Che, P. K. H. Tam, K. K. Y. Wong, *ChemMedChem* **2010**, *5*, 468.
[63] J. C. Wataha, C. T. Hanks, R. G. Craig, *Dental Materials* **1993**, *9*, 172.
[64] K. M. Pawelec, S. M. Best, R. E. Cameron, *J. Mater. Chem. B* **2016**, *4*, 6484.
[65] N. X. Landén, D. Li, M. Ståhle, *Cell. Mol. Life Sci.* **2016**, *73*, 3861.
[66] T. Fujii, S. Takayama, Y. Ito, *J. Biol. Macromolecules* **2013**, *13*, 92.
[67] J. Hudzicki, *Am. Soc. Microbiol.* **2009**, *15*, 55.

